Diffusion Weighted Magnetic Resonance Imaging in the Characterization of Soft Tissue Sarcoma

Shu Xing, MSc.

Master of Science

Faculty of Medicine

McGill University

Montreal,Quebec

2015-08

Thesis submitted to the Faculty of Graduate Studies and Research in partial fulfillment of the requirements for the degree of Master of Science

DEDICATION

To my parents who have always loved me

To Dr. Ives Levesque, who always encourages me to pursue my dreams

To all the wonderful people in my group

To you who is spending your time reading my work

ACKNOWLEDGEMENTS

I would like to thank my parents to their love and support. They have always believed in me and my dreams. I wish to acknowledge my supervisor Dr. Ives Levesque for giving me an opportunity to work with MRI and for all his inspiration, guidance and care during my degree. Also, I would like to thank Zaki Ahmed, Mikael Simard and Veronique Fortier in my research group for all the heated discussions. For financial support, I would like to acknowledge the Health and Social Services of Quebec, Medical Physics Research Training Network, and the Medical Physics Unit at the Montreal General Hospital for funding my studies. Finally, A big thanks to all my friends and colleagues who make me feel like home in Montreal. I love you all.

ABSTRACT

Diffusion weighted magnetic resonance imaging (DW-MRI) is a non-invasive imaging modality sensitive to the Brownian motion of water, which is widely used in the field of medical research and diagnostic medicine. In this work, DW-MR images were acquired in patients with diagnosed soft-tissue sarcoma at pre-, mid- and post-radiotherapy. Quantitative analysis of DW-MR images at pre-radiotherapy provided insights on the differentiation of myxoid-containing and non-myxoid containing soft-tissue lesions. Longitudinal analysis across three stages of radiotherapy allowed one to evaluate therapy response from the changes in the apparent diffusion coefficients (ADCs). In the effort to better understand tumour microenvironment, a reference region based segmentation method was proposed to automate the process of differentiating high T2 content, high cellularity tissue, necrotic tissue and fibrous tissue within the tumour. Conventionally, these tissue types were interpreted via visual inspection, based on the combinatory pattern of the relative signal intensity of the lesion to its surrounding tissue, from T2-weighted, high b-value DW images and the ADC map. In the proposed method, we avoided the signal dependence of T2-weighted and high b-value DW images, by using quantitative T2 map, ADC map and a computed surrogate map, which captured the main physical properties of high b-value DW images. This method was tested with the soft-tissue sarcoma data set. High T2 content, high cellularity tissue, necrotic tissue and fibrous tissue were successfully differentiated in each lesion.

ABRÉGÉ

L'imagerie par résonance magnétique de diffusion (DW-IRM) est une technique d'imagerie non-invasive. Elle permet de calculer en chaque point de l'image la distribution des directions de diffusion des molecules d'eau. Cette technique est largement utilisé dans le domaine de la recherche médicale et la médecine diagnostique. Dans cette thèse, les images de DW-IRM ont été acquises chez les patients ayant reu un diagnostic de sarcome des tissus mous au préalable, à moyen et post-radiothérapie. L'analyse quantitative des images de DW-IRM au pré-radiothérapie ont donné un apercu sur la différenciation des myxoid-containing et non-myxoid containing lésions de sarcome des tissus mous. La réponse de la radiothérapie a été évaluée par l'analyse longitudinale de les changements des coefficients de diffusion apparent (ADC) àtravers trois étapes de la radiothérapie. Dans le but de mieux comprendre microenvironnement de la tumeur, une méthode de segmentation a été proposé d'automatiser le processus de différenciation des tissus avec élevée en T2, tissus de haute cellularité, tissus nécrosés et du tissu fibreux dans la tumeur. Classiquement, ces types de tissus ont été interprétés par inspection visuelle, basée sur le modèle combinatoire de l'intensité de signal relative de la lésion á son tissu environnant, par d'image de T2-weighted, d'image de DW-IRM et de la cartographie d'ADC. Dans la méthode proposée, nous avons évité la dépendance du signal d'image de DW-IRM et d'images de T2-weighted, en utilisant la cartographie d'T2, la cartographie d'ADC et une cartographie de mère porteuse calculée, qui a capturé les principales propriétés physiques d'image de DW-IRM.Cette méthode a été testée

avec le tissu mou du sarcome de données ensemble. Tissus de haute T2, tissus de haute cellularité, tissus nécrosés et du tissu fibreux ont été différenciées avec succès dans chaque lesion.

TABLE OF CONTENTS

LIST OF TABLES

LIST OF FIGURES

CHAPTER 1
Introduction

"In the beginning it was all black and white" - Maureen O'Hara

Magnetic resonance imaging (MRI) is a non-invasive imaging modality widely used in the field of medical research and diagnostic medicine. The origin of MRI, or previously referred to as nuclear magnetic resonance imaging (NMRI), can be tracked back to 1946. During this time, Felix Bloch and Edward M. Purcell found that when certain nuclei were place in a magnetic field, they absorb energy and re-emit this energy when nuclei return to their original state. This phenomenon is the essence of MRI today, for which Bloch and Purcell jointly received the Nobel Prize in Physics in 1952 [1].

NMR was soon applied to create 2D images through a line scan technique, which led to the first image of in vivo human anatomy. In 1977, Raymond Damadian successfully imaged a cross section of a human chest [2]. This serves as a milestone in the development of MRI as a valuable tool for non-invasive high resolution anatomical imaging. Around the same time in 1965, Stejskal and Tanner introduced a novel MR sequence sensitive to the Brownian motion of water, known as diffusion weighted imaging (DWI).[3]. This technique allows scientists to look beyond the macroscopic

structures of the human anatomy and to characterize the diffusional movement of molecules. Since then, DWI has been widely applied to detect stroke in its acute phase, to map neuro-networks, and to understand the microenvironment of tumours [4, 5, 6, 7].

In oncologic imaging, DW-MRI is particularly advantageous due to the dynamic nature of tumours. Imagine for a moment that we could tag one of the water molecules inside the tumour and track its migration. We could see that the path taken by the water molecule is shaped by the microscopic structure of the tumour. We might observe, for example, that the water molecule is trapped among densely packed cells, in the case of malignant lesions; we might see that the water molecule moves more freely in benign or normal tissues; or it can be completely unrestricted in a cell free region such as necrotic areas. The path of the water molecule therefore reflects the microscopic environment of the tumour and its composition. These information are crucial for delineating subregions that may benefit from higher radiotherapy doses as well as for treatment monitoring.

The topic of interest in this thesis is to use DWI for better understanding of soft-tissue sarcoma, a rare heterogeneous group of tumours arising from mesenchymal tissues that occur at all ages from childhood and adolescence up to the elderly. MRI is the best imaging modality for this type of tumour due to its excellent soft tissue contrast. As part of a multi-modal imaging study, conventional T2-weighted and diffusion weighted images were acquired in 10 patients with diagnosed soft-tissue sarcoma before, during and after pre-operative radiotherapy. This work aims to

evaluate tumour response at these three time points and to better understand the microenvironment of soft-tissue sarcoma.

This thesis contains three main chapters. A brief overview of certain essential principles of magnetic resonance imaging is presented in Chapter 2, where a detailed review of diffusion weighted MRI and the physiology of soft-tissue sarcoma are also introduced. Chapter 3 presents the preliminary findings on the characterization of soft-tissue lesions and their radiotherapy response through quantitative analysis of the apparent diffusion coefficient (ADC). Chapter 4, presented in a manuscript format, addresses the second objective of this study - to assess the microenvironment and the subregions of the tumour. Conventionally, tumour tissue segmentations are performed by visual inspection from the physicians, which is time consuming. A novel method is proposed here to automate the tissue segmentation process and tested on the sarcoma data set. Chapter 5 concludes the study with a summary discussion of the major findings.

CHAPTER 2
Background

"People without the knowledge of their past history, origin and culture is like a tree without roots." -Marcus Garvey

2.1 Nuclear Magnetic Resonance

Magnetic resonance imaging (MRI) is a powerful noninvasive imaging modality that has widespread applications in research and clinical medicine. One could get a sense about the underlying principles of MRI from its name. The word "Magnetic" refers to the use of an assortment of magnetic fields and "resonance" refers to the need to match the radiofrequency of an oscillating magnetic field to the precessional frequency of the spin of some nucleus in a tissue molecule. MRI could be more accurately named as nuclear magnetic resonance imaging (NMRI), however, due to the general concern over the word "nuclear", this word has been suppressed [8]. Given the complexity of nuclear magnetic resonance (NMR), a quantum mechanical description is necessary to fully understand the principle of MRI. Nonetheless, in the scope of this thesis, classical concepts are sufficient to provide a clear understanding on the basics of MRI. This section provides a brief overview of the classical description of NMR physics with some quantum mechanical descriptions included when

appropriate. The concepts described here are based on the book written by Dwight G. Nishimura [9].

2.1.1 Spin

Spin is a form of angular momentum. Unlike the classical angular momentum, it is not produced by a rotation of the particle, but is an intrinsic property of the particle itself. Every elementary particle, such as electrons and quarks, has a particular spin quantum number s. $s = \frac{1}{2}$ for electrons and quarks. Protons and neutrons are both composed of three quarks, stuck together by gluons [10]. Protons have spin of $\frac{1}{2}$ due to the combinations of quark spins. For instance, when two of the quark spins are antiparallel, a net spin of zero is obtained. The additional third quark spin gives a total net spin of $\frac{1}{2}$ to the proton. Similarly, neutrons also have a net spin of $\frac{1}{2}$ for the same reason.

On an atomic level, most atomic nuclei possess spin. The nuclear spin quantum number depends on the combination of proton and neutron spins, and is conventionally denoted as I. Consider for a moment the nucleus of a hydrogen atom, ^{1}H, which contains a single proton. The nuclear spin, in this case, is equal to the net proton spin of $\frac{1}{2}$. On the other hand, a nucleus that contains even numbers of protons and neutrons would result in a nuclear spin of 0. For example the nucleus of ^{16}O contains eight protons and eight neutrons. The net proton and neutron spins are both 0, resulting a spin I=0 for the nucleus.

The spin angular momentum is a vector quantity which is expressed as

$$\mathbf{S} = \hbar\mathbf{I} \tag{2.1}$$

where $\hbar$ is Planck's constant divided by 2π and $\mathbf{I}$ is the spin operator in quantum mechanics. Associated with $\mathbf{S}$ is a magnetic dipole moment $\boldsymbol{\mu}$, which can be expressed as

$$\boldsymbol{\mu} = \gamma \mathbf{S} = \gamma \hbar \mathbf{I} \tag{2.2}$$

where, γ is the gyromagnetic ratio, a known constant unique for different nuclear species [9]. One can therefore see from Equation 2.2 that for a nucleus to have nonzero magnetic dipole moment, the spin angular moment $\mathbf{S} \neq 0$. In other words, a nucleus must have an odd number of protons and/or an odd number of neutrons to create a magnetic dipole moment. These nuclei are referred to as MR active nuclei [11]. Important examples of MR active nuclei include ^{1}H, ^{13}C, ^{15}N, ^{17}O, ^{19}F, ^{23}Na, and ^{31}P.

The hydrogen nucleus ^{1}H is the MR active nucleus used in clinical MRI, because of its abundance in the human body (in H_2O). ^{1}H contains a single proton with nuclear spin of $\frac{1}{2}$. Also, a solitary proton gives the ^{1}H a relatively large magnetic moment [11]. Both of these features enable utilization of the maximum amount of available magnetization in the body.

2.1.2 Classical Description of Nuclear Magnetism

The spin angular momentum provided a quantum mechanical explanation to the induction of magnetic moment, which can also be described with classical theory. Faraday's Law of Induction states that a magnetic field is created when a charged particle moves [12]. The hydrogen nucleus ^{1}H contains one single proton with a positive charge of +e. When a ^{1}H nucleus moves, a magnetic field is induced around it. The hydrogen nucleus therefore acts as a small magnet, similar to a permanent

magnet, illustrated in Figure 2–1. The magnetic moment has a direction along the north/south direction, which is conventionally used in the classical description of MRI. While it is easier to grasp the induction of magnetic field concept by imagining a spinning hydrogen nucleus in terms of classical electromagnetic phenomena, it is important to remember that the nuclear magnetism is in fact a quantum mechanical phenomenon. No evidence has suggested that nuclear particles actually spin in the physical sense.

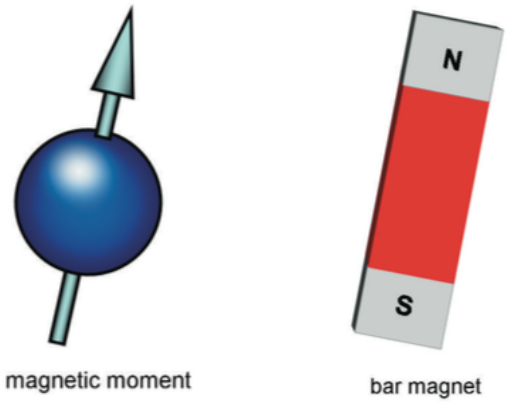

(a) (b)

Figure 2–1: The magnetic moment of the hydrogen nucleus. This figure is adapted from Westbrook et al. 2011 [11].

2.1.3 Interaction with a Static Magnetic Field

In the absence of an external magnetic field, the magnetic moments of MR active nuclei, for instance ^{1}H nuclei are randomly oriented, as illustrated in Figure 2–2. When a static magnetic field $\boldsymbol{B_0}$ is applied in the z-direction, two important effects arise: alignment and precession.

Alignment

In the presence of an external magnetic field, $\boldsymbol{B_0}$, the magnetic moments $\boldsymbol{\mu}$ of all the ^{1}H nuclei align in the direction of the applied field. As shown in Figure 2–2, some of the hydrogen nuclei align parallel with $\boldsymbol{B_0}$ and the others align antiparallel to $\boldsymbol{B_0}$, depending on the low and high energy state of the nuclei, respectively. The number of nuclei parallel to $\boldsymbol{B_0}$ is denoted as n_+, where as the number of antiparallel nuclei is denoted as n_-.

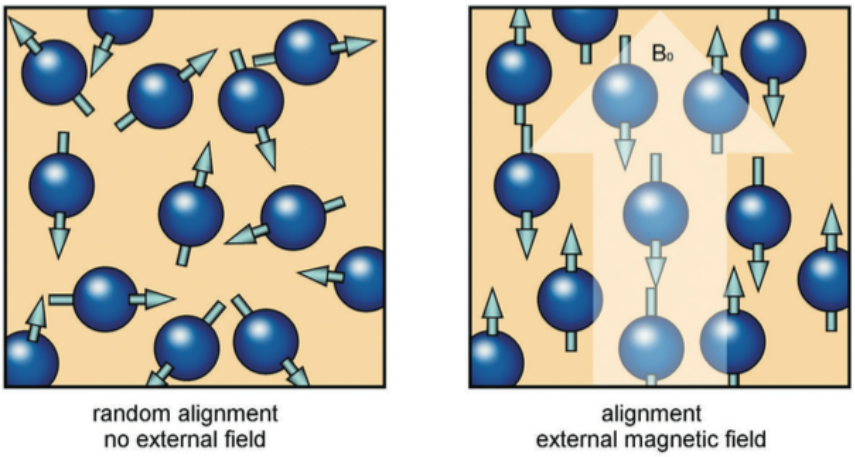

Figure 2–2: Schematic graph shows a classical description of alignment. This figure is adapted from Westbrook et al. 2011 [11].

The energy difference between these two states can be expressed as

$$\Delta E = \gamma \hbar B_0 \tag{2.3}$$

Since n_+ population occupies a lower energy state, more nuclei tend to join this population. However, thermal energy is sufficient to ensure that the higher energy

state is also occupied. The ratio of the two population can be described by the Boltzmann distribution:

$$\frac{n_-}{n_+} = e^{-\Delta E/kT} \tag{2.4}$$

where k is Boltzmann's constant and T is the absolute temperature. Macroscopically, the excess in n_+ population creates a net magnetization $\mathbf{M}$ in the same direction as $\boldsymbol{B_0}$, where $\mathbf{M}=\sum \boldsymbol{\mu}$.

Precession

When $\mathbf{M}$ is tipped away from the direction of $\boldsymbol{B_0}$, the magnetic field impinges a torque on the nuclear magnetic moment of each hydrogen nucleus. The effect of torque induces a precession of the magnetic moment about the applied field $\boldsymbol{B_0}$ (Figure 2–3, adapted from [13]). This precession is analogous to the nutation of a spinning top in a gravitational field when it is tilted slightly off axis.

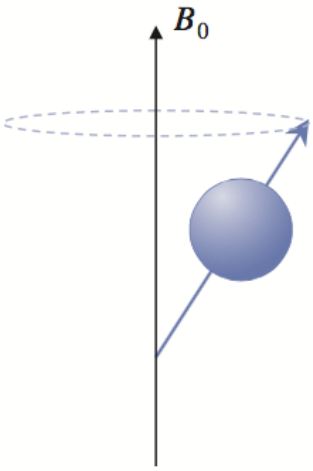

Figure 2–3: Precession of the magnetic moment. This figure is adapted from [13].

The torque equals to the rate of change of angular momentum which can be expressed as

$$\frac{d\mathbf{S}}{dt} = \boldsymbol{\mu} \times \mathbf{B} \tag{2.5}$$

or if both sides are multiplied by γ:

$$\frac{d\boldsymbol{\mu}}{dt} = \boldsymbol{\mu} \times \gamma\mathbf{B} \tag{2.6}$$

The precession of individual nucleus causes a precession in the net magnetization around the $\boldsymbol{B_0}$ field. Its equation of motion can be expressed as

$$\frac{d\mathbf{M}}{dt} = \mathbf{M} \times \gamma\mathbf{B} \tag{2.7}$$

The solution to this equation gives the precession resonance frequency of $\mathbf{M}$, which is referred to as the Larmor frequency.

$$\omega = \gamma B \tag{2.8}$$

As the gyromagnetic ratio γ is an unique constant for each nuclide that has a nuclear magnetic moment, the Larmor frequency is constant for a given magnetic field. For ^{1}H, $\gamma/2\pi = 42.58$ MHz/T.

2.1.4 Interaction with a Radiofrequency Field

In order to obtain a MR signal, a radiofrequency (RF) magnetic field $\boldsymbol{B_1}$ in the xy transverse plane, tuned to the resonance frequency of the spins, is applied. Some low energy nuclei absorb the energy from the RF field and join the high energy population. This causes the net magnetization $\mathbf{M}$ to rotate away from the longitudinal z axis, into the xy plane, as demonstrated in Figure 2–4. A rotating frame of

reference is often used to picture this phenomenon. When the axes are rotating at the resonance frequency of the spins, the **M** simply flips down to the xy plane. This behaviour is termed excitation. The resulting flip angle is a function of B_1 and its duration τ, given by $\Delta\theta = \gamma B_1 \tau$. The flip angle is typically 90^o, because it leads to the largest possible signal in the xy plane.

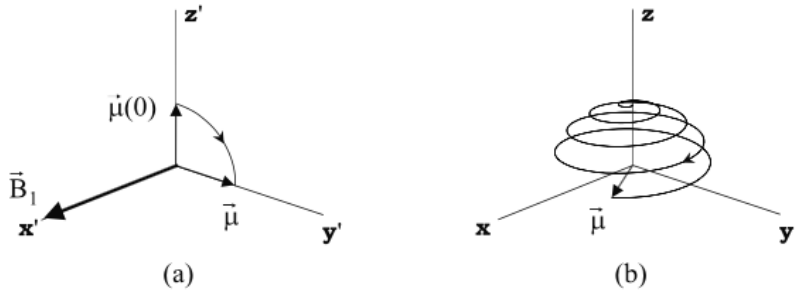

Figure 2–4: (a) In a rotating frame of reference, the net magnetization **M** is tipped down to the transverse xy plane due to $\boldsymbol{B_1}$. (b) In a laboratory frame, the axis is also rotating, making the $\boldsymbol{B_1}$ induced rotation of magnetization towards transverse plane more complicated. This figure is adapted from [8].

2.1.5 Relaxation effects

After $\boldsymbol{B_1}$ is turned off, the net magnetization **M** with the magnitude of M_0 continues to precess in the xy plane about the z-axis. However, **M** eventually returns to realign with $\boldsymbol{B_0}$ along the z-axis and restore its original magnitude of M_0. Two important processes are happening during this time: longitudinal T_1 recovery and transverse T_2 decay.

T_1 recovery refers to the recovery of the longitudinal magnetization, i.e. M_z to M_0, which behaves according to

$$\frac{dM_z}{dt} = -\frac{M_z - M_0}{T_1} \tag{2.9}$$

During this process, nuclei give up their energy to the surrounding lattice and return to their original energy state. Therefore, T_1 recovery is also named spin lattice relaxation. The rate of recovery follows an exponential trend, with a recovery time constant termed T_1 relaxation time. Following a 90^o excitation, T_1 recovery can be expressed as:

$$M_z = M_0(1 - e^{t/T_1}) \tag{2.10}$$

T_2 decay, on the other hand, refers to the decay of transverse magnetization, i.e. M_{xy} to 0. The transverse magnetization behaves according to

$$\frac{dM_{xy}}{dt} = -\frac{M_{xy}}{T_2} \tag{2.11}$$

This process is a result of neighbouring nuclei interacting with each other causing the loss of phase coherence (dephasing) of the transverse magnetization. T_2 decay is therefore also termed spin-spin relaxation. The rate of decay can also be described with an exponential function

$$M_{xy} = M_0(e^{-t/T_2}) \tag{2.12}$$

where, T_2 is the decay constant, named T_2 relaxation time.

In addition, the external field inhomogeneities also contribute to the decay of the transverse magnetization. The observed decay time $T_2{}^*$ is therefore shorter than

T_2, given by

$$\frac{1}{T_2*} = \frac{1}{T_2} + \frac{1}{T_2'} \tag{2.13}$$

where T_2' accounts for the decay time due to field inhomogeneity. This effect is reversible by refocusing M_{xy} with another RF excitation pulse (magnetic field). This type of combination is often referred to as the spin-echo sequence. To measure the true T_2 effect, one has to run the spin-echo sequence multiple times or the multi-echo sequence, where more than one additional RF excitation pulse are applied.

2.1.6 Signal Detection

Signal detection occurs after the RF excitation pulse is turned off. The magnetization continues to process in the xy plane with the Larmor frequency of the spins. A rotating magnetic moment generates a rotating magnetic field, which in turn produces an electromotive force (EMF), according to Faraday's law of induction. The same RF coil used to generate the RF excitation pulse $\boldsymbol{B_1}$is used to detect the EMF. The resulting basic MRI signal is called the free induction decay (FID). It is important to realize that the receiver coil only detects signal generated from the transverse magnetization. As T_1 and T_2 relaxation effects take place, the signal amplitude decreases. FID is thereby a time dependent signal, that decays with the relaxation time T_2*, as illustrated in Figure 2–5.

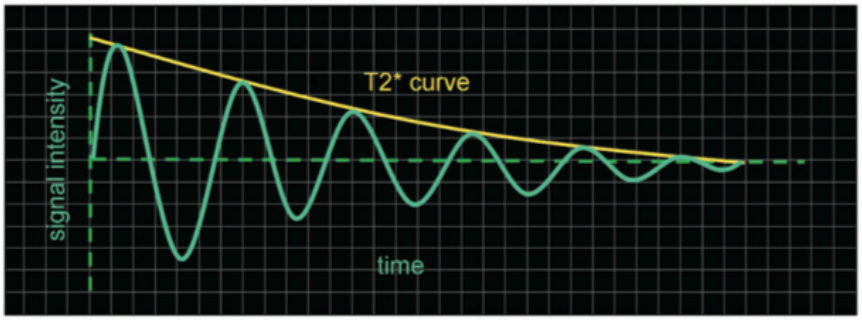

Figure 2–5: Schematics of a FID curve with T_2* decay. This figure is adapted from [11].

2.1.7 Gradient field

The essence of MRI is based on the interaction MR active nuclei with three types of magnetic fields. We have introduced the interaction of spin with an external magnetic field and a radiofrequency field. The last type of magnetic field discussed here is the gradient field G.

A gradient field is a field strength variation on the $\boldsymbol{B_0}$ field. The simplest but most common case of gradient field is the linear gradient magnetic field, which is a field along the same direction as $\boldsymbol{B_0}$, but with an amplitude that varies with position. For instance, when an x-gradient G_x is applied, the external magnetic field now has a position dependence on x. Hence,

$$B_z = B_0 + G_x x \tag{2.14}$$

where $G_x = \mathrm{d}B_z/\mathrm{dx}$ with a unit of T/m. It is crucial to remember that the combined magnetic field remains in the z-direction, only the field strength varies with the x-location. More importantly, the precession frequency of the nuclei now has a x location dependence, according to the Larmor equation (Eq. 2.8), expressed as

$$\omega(x) = \gamma(B_0 + G_x x) = \omega_0 + \gamma G_x x \tag{2.15}$$

When a gradient is on, the spins precess faster as the combined magnetic field increases, and slower when the combined magnetic field decreases. This behaviour allows us to induce spin dephasing and rephasing without waiting for the natural spin dephasing due to T_2 relaxation or a 180^o RF excitation pulse. Spin dephasing refers to the lose of phase coherence, whereas spin rephasing refers to the restoration of phase coherence. Figure 2–6 illustrates the mechanism of gradient induced spin dephasing and rephasing.

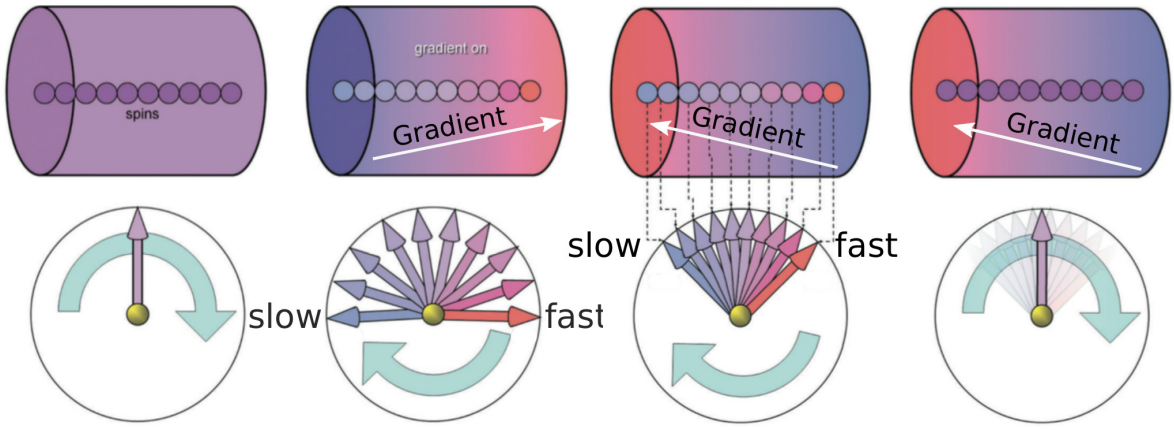

Figure 2–6: This schematic demonstrates spin dephasing and rephasing due to the presence of gradient fields. This figure is adapted from [11].

If no gradient field is applied, all spins precess at the same Larmor frequency ω_0. When a positive gradient is applied along the x-direction, the spins further along the gradient axis precess faster than those near the origin. For simplicity, we refer them as fast spins and slow spins respectively. As a result, the magnetic moments fan out or dephase, just like when the spins lose their phase coherence during T_2 relaxation. Now, if a negative gradient of the same magnitude is applied along the x-direction, the fast spins are slowing down due to the decreased magnetic field further along the axis. Similarly, the slow spins are precessing faster, owing to the increased magnetic field near the origin. Eventually, the slow spins catch up with the fast spins. Phase coherence is thus restored. A number of imaging sequences use gradient induced dephasing and rephasing, such as gradient echo and diffusion weighted spin echo sequences. In fact, this is the very effect that led Stejskal and Tanner to the design of diffusion weighted spin echo sequence, which is described in the next section.

2.2 Diffusion Weighted MRI

Seventy two percent of the human body is composed of water. While water appears static to the naked eye, water molecules are in constant random motion at the microscopic level. This phenomenon is commonly referred to as Brownian motion, named after the Scottish botanist Robert Brown who first observed that particles trapped in pollen grains move through water in 1827. It was not until Albert Einstein published a paper in 1905, that it became clear that the pollen grains were moved by individual water molecules due to their thermal agitation [14]. The random water motion is also termed diffusion. In biological tissues, diffusion is not completely random. Water diffusion can be hindered by cell membranes, vascular

structures or macromolecules. Thus, measuring water diffusion enables us to gain insights about the tissue structure without actually seeing it.

2.2.1 Theory of Diffusion Weighted MRI

In 1965, Stejskal and Tanner introduced an MR sequence sensitive to the Brownian motion of water, as illustrated in Figure 2–7 [3]. This sequence consists of a 90^o RF excitation pulse, a 180^o RF pulse and two gradient pulses. The 90^o RF excitation pulse brings the net magnetization into the transverse plane. The first gradient is applied right after this RF pulse causing spins to dephase depending on the combined external field they experience. The concept of gradient induced dephasing and rephasing is explained in section 2.1.7. In Figure 2–7, the green, orange and blue filled circles represent spins at different locations along the gradient. For demonstration purposes, we call them fast, medium and slow spins respectively. After the gradient is turned off, the spins evolve freely. Static spins stay in the same position while moving spins change their relative position. A 180^o RF pulse is then applied, flipping the phase of all spins to the opposite direction. At this moment, the slow spins are leading the medium and the fast spins, in the case of static spins. If the medium spins have switched position with the slow spins, however, the medium spins would now lead the slow and the fast spins. Then, another identical gradient is used to rephase the spins. The static spins restore their phase coherence, as the fast spins catch up with the slow spins, neglecting T_2 relaxation effects. The moving spins, on the other hand, do not recover their phase coherence completely, because now the slow, medium and fast spins each have a different phase. As a result, the acquired signal from the moving spins is lower than the one from the static spins.

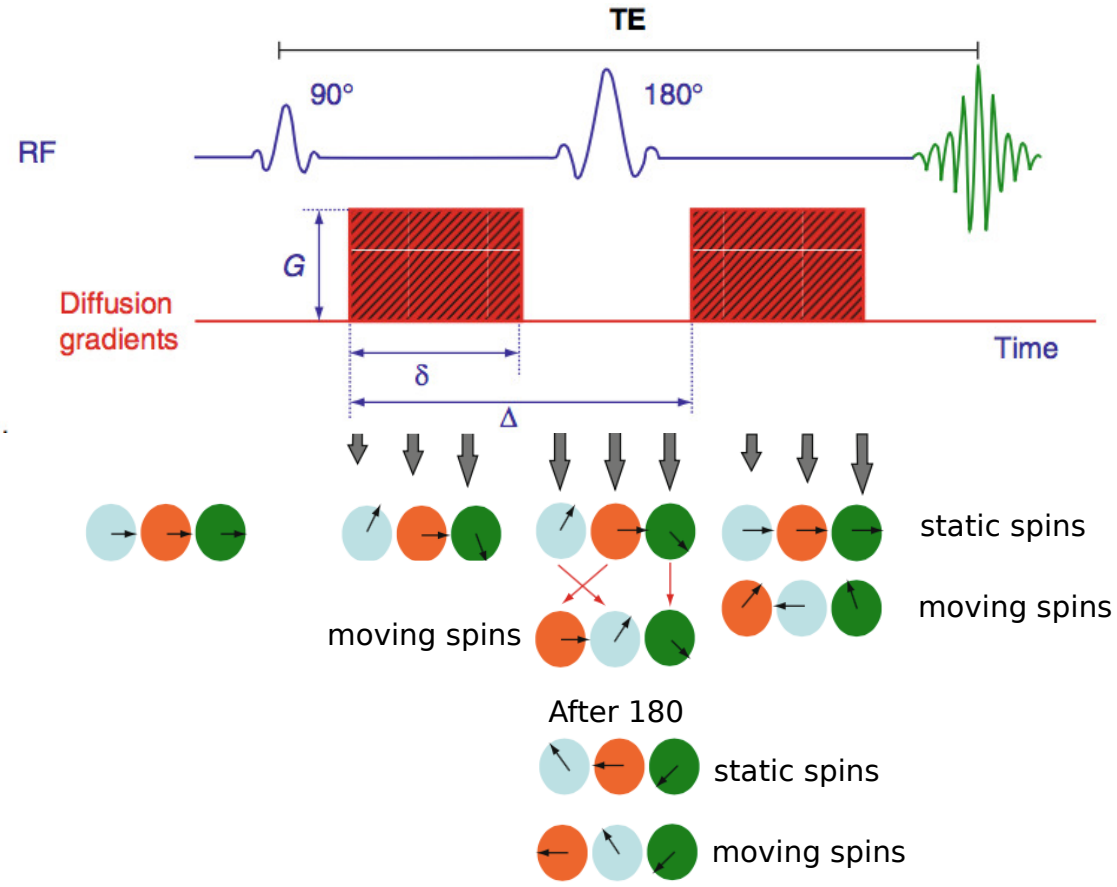

Figure 2–7: Schematic representation of the DW-MR sequence of Stejskal and Tanner. This sequence which uses two lobe gradients is sensitive to Brownian water motion. The introduction of diffusion weighting illustrated by the green, orange and blue filled circles representing spins at different locations. G represents the strength of the gradient. δ is a measure of the gradient duration. Δ represents the time interval between the two gradient lobes. This figure is adapted from [15].

2.2.2 Quantitative Analysis of DWI

Stejskal and Tanner realized that the signal loss from their sequence depends on the gyromagnetic constant γ, the gradient intensity G, the application time of the gradient γ, the time separation between the two applied gradients Δ and the diffusion coefficient D. They derived the reduction in signal related to the amount of diffusion through the following equation [3].

$$\frac{S(TE)}{S_0} = exp[-\gamma^2 G^2 \delta^2 (\Delta - \frac{\delta}{3}) D] \tag{2.16}$$

where S_0 is the signal intensity without the diffusion weighting and S being the signal with nonzero gradients. In 1985, Le Bihan suggested to simplify this equation by gathering all the gradient terms in a "b factor" [15]. The b factor is expressed in Equation 2.17, which only depend on the acquisition parameters.

$$b = \gamma^2 G^2 \delta^2 (\Delta - \frac{\delta}{3}) \tag{2.17}$$

As a result, the signal reduction equation can be simplified to

$$S(b, TE)_{SE} = S(b_0) \cdot exp(-b \cdot ADC) \tag{2.18}$$

D is replaced with the apparent diffusion coefficient (ADC) to indicate that the water diffusion is not completely free in tissue, but restricted by many mechanisms. Taking the natural logarithm of both sides, ADC can be computed with

$$ADC = -\frac{1}{(b - b_0)} ln(\frac{S(b)}{S(b_0)}) \tag{2.19}$$

It is important to note that the ADC is no long MR signal dependent, but reflects the intrinsic diffusion properties of a given tissue. In this case, the MR scanner acts as a measuring instrument extracting physical parameters instead of behaving like a camera. The ADC concept has a variety of clinical applications.

2.2.3 Clinical Applications of Diffusion Weighted MRI

The first clinical application of Diffusion Weighted MRI was reported in 1990, when Moseley et al. found that diffusion weighted imaging in a cat brain allowed the detection of ischemic brain areas in the first 30 mins [16]. Around the same time, Le Bihan et al. suggested that brain perfusion could be viewed as a pseudo-diffusion process and approximated with the intravoxel incoherent motion model (IVIM) [17]. Over the years, DW-MRI has become a valuable tool for stroke detection, mapping of the brain structures and the understanding of pathophysiological mechanisms of multiple sclerosis [18, 19, 20, 21]. In recent years, application of DW-MRI has attracted attention in the field of oncology for lesion detection, diagnosis, monitoring of treatment response and characterization of tumour tissue properties. Figure 2–8 provides an example of DW-MRI aided tumour detection [22]. On the T2-weighted image, the lesion pointed by the white triangle is difficult to spot. On the b=$750s/mm^2$ DW-MR image, however, the tumour appears bright and stands out from its surrounding tissue. This is due to the fact that malignant tissues tend to have greater cellularity, leading to more restricted water motion, which causes less signal reduction on DW-MR images. Restricted diffusion also leads to low ADC values. The location of the lesion is further confirmed by the ADC map.

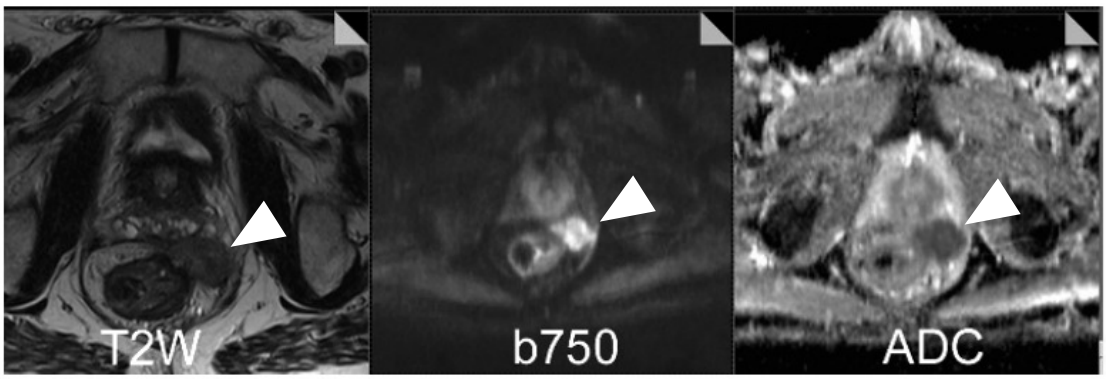

Figure 2–8: Restricted diffusion within rectal cancer with extension into the perirectal space. T2-weighted image demonstrates lesion in perirectal space. Diffusion-weighted image obtained at a b value of 750 s/mm^2 yields a high signal and corresponding ADC map demonstrates restricted diffusion within the tumour. This figure is adapted from [23].

The other important application of DW-MRI is tissue characterization. Studies have reported reduced ADCs in malignant lesions compared to benign and normal tissue. For instance, DW-MRI is able to differentiate between benign and malignant breast tumours based on their ADC values [23, 24]. Another study on focal hepatic lesions reports similar results, with ADC of benign lesions being significantly higher than those of malignant lesions [25]. In addition, DW-MRI is used for assessing tumour response to chemotherapy and radiotherapy. The therapy-induced increase in ADC has been demonstrated in multiple literatures and is considered a sign for cell lysis and necrosis, which reflects successful treatment [26, 27, 28]. Furthermore, DW-MRI is also useful in tumour staging and prediction of therapy outcomes, which

are not discussed here. Due to its many applications, DW-MR imaging is now part of the clinical imaging routine at many institutions.

2.3 Automated MRI-based tumour Segmentation

Another important oncological application of MRI is tumour segmentation. Modern radiation therapy treatment techniques such as intensity modulated radiation therapy allows for precise dose application. In order to take full advantage of such technique, an accurate tumour volume delineation is highly beneficial [29]. Many literatures have reported automated or semi-automated MRI-based tumour segmentation algorithms, especially on brain tumours [30]. Most segmentation algorithms include three major steps: image pre-precessing, feature extraction, and segmentation.

Besides anatomical variation, MRI signal intensity is inhomogeneous due to radio-frequency field non-uniformity and eddy currents resulted from switching gradient fields in the imaging system. Therefore, most segmentation algorithms rely on certain pre-processing to correct for intensity inhomogeneity [31]. A simple normalization method is to standardize the mean or the median intensity of the volume of interest. An improved approach computes the intensity percentile of several predefined landmark regions relative to the intensity histogram of the input and maps these landmarks to pre-defined standard percentile values [32]. More sophisticated algorithms have also been developed, including non-parametric non-uniform intensity normalization and bias-field correction [33]. Imaging denoising is another standard pre-processing task, where a de-noising filter, such as gaussian filter, anisotropic diffusion filter, is applied to the image to reduce noise [34]. For segmentation with

multi-modal images, pre-processing also includes registration of all modalities in a common space of reference.

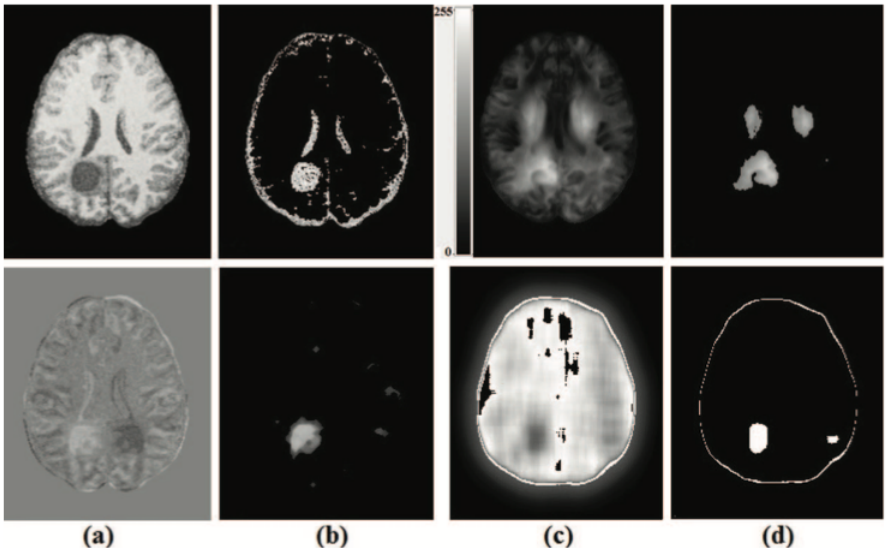

Figure 2–9: Features extracted from a T1 MRI with simulated tumour. Top row: (a) Normalized intensity, (b) Thresholded intensity feature, (c) Deformation field magnitude, (d) Thresholded deformation feature; Bottom row: (a) Subtraction of image and reflected image through symmetry plane, (b) Thresholded and filtered symmetry feature, (c) Windowed Gabor-filtered image, (d) Thresholded texture feature [31].

The next major step of tumour segmentation algorithms is selecting image features. The segmentation features used for brain tumours largely depend on the tumour type and grade. Most common features include intensity, symmetry, shape deformation and textures. Figure 2–9 demonstrates theses features extracted from a T_1-weighted image with a simulated tumour and the resulting feature images [31]. Intensity thresholding has been widely used for tumour segmentation (top row (a)

(b)), but it is often insufficient for robust tumour detection. Symmetry feature, on the other hand, has shown to be more robust for tumour segmentation [35]. Healthy brain has a high degree of symmetry between two hemispheres. The presence of tumour causes asymmetry in the brain anatomy, which could be used to detect the tumour (bottom row (a) (b)). Shape deformation feature captures the anatomical deformation in the surrounding structure caused by tumour growth. The magnitude of deformation can be calculated and thresholded for tumour detection. Lastly, texture analysis is an important method and has a lengthy history in automated tumour segmentation. In 1993, German scientist Schard et al. first applied texture analysis to T_1 and T_2 images and demonstrated promising results for in vivo tissue segmentation [36]. Common texture parameters include mean/variance of grey levels, skewness, contrast, homogeneity, entropy and the grey level co-occurrence matrix.

Based on the extracted features, segmentation algorithms are applied to differentiate tumours from health tissue. Most of the segmentation algorithms proposed uses classification or clustering approach, which can easily handle multi-modal datasets. Classification requires training data sets to learn a classification model, from which new data sets can be classified. Each voxel is decided individually to which class it belongs to based on a given image feature [30]. On the other hand, clustering works in an unsupervised way and groups data based on similarity in certain features[37]. Clustering was first introduced into brain tumour segmentation by the same german scientist Schard et al., who applied texture analysis to T_1 and T_2 brain images. In 1995, Phillips et al applied fuzzy c-means clustering which is still used today [38].

Recently, Cai et al employed a number of MRI modalities including diffusion tensor imaging, T_1 and T_2 imaging to create voxel-wise intensity-based feature vectors. They were able to not only differentiate tumour from health tissues, but also segment sub-compartment of tumour regions including necrosis, edema and active cells [39].

MRI-based tumour segmentation algorithms have also been applied to tumour sites outside of the brain, including head and neck, breast, and prostate cancer [40, 41, 29].

2.4 Soft-tissue sarcoma

2.4.1 Overview of soft-tissue sarcoma

Soft tissue arises from the mesenchyme, which differentiates during development to become fat, skeletal muscle, peripheral nerves, blood vessels and fibrous tissue [42]. 3Soft-tissue sarcoma comprise a heterogeneous group of tumours arising from soft tissue. They are rare tumours representing 1% of all cancers in adults and approximately 7% of all childhood malignancies [43]. The World Health Organization (WHO) classifies soft-tissue sarcoma into nine categories: adipocytic, fibroblastic/myofibroblastic, fibrohistiocytic, smooth muscle vascular, chondro-osseous and those of uncertain differentiation [44]. Over 50% of soft-tissue sarcomas begin in the limbs [43]. They occur most often in the thigh. The most frequent histologic types occurring in this location are pleomorphic undifferentiated sarcomas, liposarcomas and leiomyosarcomas [45].

MR imaging is advantageous for the diagnosis and evaluation of soft-tissue sarcoma, due to its high soft tissue contrast. T1-weighted and T2-weighted imaging sequence are typically used to provides information about the size and location of

the tumour as well as its relationship to other structures [46]. A complementary CT scan may also be performed to check for pulmonary metastases and to evaluate the presence of bone involvement. Biopsy is generally performed to confirm the diagnosis and determine the tumour grade and histology [43].

Traditionally, local surgical excision is used as the sole therapy for soft-tissue sarcoma [47]. Nevertheless, due to the high local recurrence rate of 30 to 50% after local surgical excision, radical compartmental excision or amputation became the standard practice to achieve local control rate of 80-90% and to reduce local recurrence rate to 5 to 20% [48]. Increasing local control at the expense of limb preservation is far from ideal, as it decreases patients' quality of life. Recently, a study of 43 adult patients with high grade soft-tissue sarcoma of the extremities was conducted by the US National Cancer Institute, where they were prospectively randomized to receive either amputation or limb-sparing resection with radiotherapy. They have reported four local recurrences in the limb-sparing group and none in the amputation group. However, there were no differences in survival rates between these two groups [49]. As a result, the current preferred management of soft-tissue sarcoma is conservative surgery and radiotherapy. The rationale for combining radiotherapy with surgery is that radiotherapy eradicates microscopic disease allowing more conservative surgery with equal probability of local control and survival [49]. Increasingly, radiotherapy is also given preoperatively, for reducing the tumour volume to a more manageable level for surgical resection [50]. For higher stage tumours with distant metastases, chemotherapy may be given in combination of radiotherapy, before and/or after surgery. A prospective randomized study of postoperative

chemotherapy in 65 patients with high-grade soft-tissue sarcomas of the extremities revealed a significant increase of overall survival rate in patients received chemotherapy(95% survival rate) compared to those without chemotherapy (74% survival rate) [49].

2.4.2 Application of Diffusion weighted MRI to soft tissue sarcoma

Application of diffusion weighted MRI and quantitative analysis to characterize soft-tissue sarcoma has been reported, mainly focused on the differentiation of malignant from benign soft-tissue tumours [51, 52]. Lee et al. assessed the malignancy of soft-tissue tumours via visual inspection from two separate radiologists. tumour intensity was compared with that of surrounding muscle and scored from grade one to four, with one being hypo-intense relative to muscle and four being iso-intense to fluid. It was reported that grade four tumours were more common in malignant tumours. The minimum apparent diffusion coefficient (ADC) of the tumour and the minimum ADC over the average ADC for normal muscle demonstrated statistically significant difference between malignant tumours and non-malignant ones [51]. A similar method of differentiating malignant from benign soft-tissue tumours was proposed by Teixeira et al [52]. The tumours were visually classified into hypo-intense, iso-intense and hyper-intense, based on T_2-weighted images. Muscle was again used as a reference tissue, where its ADCs from both benign and malignant groups were obtained. Similarly, the ADC ratio between min tumour ADC and average muscle ADC was calculated for each voxel. Benign tumours were differentiated from malignant tumours with high sensitivity and specificity for T_2 hyper-intense tumours.

Previous literature findings demonstrated that the addition of qualitative and quantitative DWI to standard MRI protocol improves diagnostic accuracy for differentiation between malignant and benign soft-tissue tumours. However, both example analysis mentioned above still contain a qualitative component, carried out via visual inspection. Moreover, no one to our knowledge has reported automated soft-tissue tumour sub-region segmentation method. The major finding presented in this thesis (chapter 4) successfully automated tumour sub-region segmentation employing quantitative T_2 and ADC, which serves as a step-forward to further understand the microenvironment of soft-tissue tumour and to provide essential information for sub-region targeted radiation dose painting.

CHAPTER 3
Quantitative analysis of diffusion weighted imaging in soft-tissue sarcoma

"He will turn himself into every kind of creature that goes upon the earth, and will become also both fire and water; But you must hold him fast and grip him tighter and tighter, till he begins to talk to you and comes back to what he was when you saw him go to sleep." - Homer, Odyssey

3.1 Introduction

The superior soft tissue contrast of MRI makes it the ideal imaging modality for studying soft-tissue sarcoma. As the name suggests, it is a type of cancer that originates from the soft tissues of the body. Diffusion weighted-MRI (DW-MRI) is sensitive to the Brownian motion of water, thereby provides useful insights on the tumour microenvironment. Water diffusivity, i.e. the rate of diffusion, can be quantified as the isotropic apparent diffusion coefficient (ADC) in the form of a parametric map. In general, malignant tumours have lower ADCs compared to normal tissue owing to their increased cellularity. In the case of soft-tissue sarcoma, however, malignant lesions sometimes demonstrate elevated ADCs. This is thought to be due to the high heterogeneity and variability of composition of soft-tissue tumours. For instance, Maeda et al have reported increased ADCs from myxoid

tumours, due to the presence of the myxoid matrix where free water is abundant in the extracellular space [53].

A few studies have explored the post-therapeutic change in soft-tissue tumours using quantitative analysis of DWI. Increase in ADC was reported to be positively correlated with response to radiotherapy, associated with reduction in tumour size and tumour cellularity [54, 55, 56]. However, the relationship between ADC and tumour characteristics or radiotherapy response is still poorly understood. An ongoing clinical study on the role of fludeoxyglucose positron emission tomography (FDG-PET), fluoromisonidazole PET (FMISO-PET) and DW-MRI in the management of soft-tissue sarcoma of the extremities with pre-operative radiotherapy and surgery were conducted by a team of researchers from the McGill University Health Center. DW-MR data were acquired in patients at three stages of treatment: pre-, mid- and post-radiotherapy. With these data, we further explore the relationship between ADC and tumour types, change in ADC and response to radiotherapy, as well as post-therapeutic change in ADC and tumour location. The findings are reported in this chapter.

3.2 Method

3.2.1 Patient

From October 2013 to January 2015, 10 patients (4 females and 6 males; age range 48-81 years) were recruited with histologically confirmed soft-tissue sarcoma to participate in this clinical study. All tumours were malignant including three undifferentiated pleomorphic spindle cell sarcoma (UPS), two myxoid liposarcoma, one myxoid/round cell liposarcoma, one leiomyosarcoma, one myxofibrosarcoma,

one pleomorphic liposarcoma and one synovial sarcoma. Lesions were located in the shoulder(2), leg(1), thigh(3), arm(2), pelvis(1), and chest wall (1). Recruited patients satisfied the following criteria: (a) A biopsy must be done within 8 weeks prior to registration. (b) The tumour must be surgically resectable. (c) The patient must be fit for surgery. (d) The patient must be at least 18 years old. (e) For females with childbearing potential, a serum βHCG must be done 2 weeks prior to registration and the patient must practice adequate contraception. Patients with rhabdomyosarcoma, Ewing sarcoma, osteosarcoma and Kaposi sarcoma, metallic objects in the body, prior radiotherapy or excisional biopsy leading to the removal of the majority of the tumour were excluded from this study. The study was approved by the Research Ethics Board of the McGill University Health Center and written informed consent was obtained from each patient.

3.2.2 MRI

Echo planar imaging (EPI) based DW-MR images were acquired with a 1.5 T MR scanner (GE Healthcare, Waukesha WI, USA) at b = 0, 100, 500, 800 s/mm^2 in 8 out of 10 patients in week 1 of the study prior to radiotherapy. 6 out of these 8 patients have completed the DW-MRI at all three stages of the radiotherapy course: pre-(week 1), intra-(week 4) and post-radiotherapy (week 9). All 10 patients received surgery in week 10. The field-of-view, number of slices and slice thickness were adapted for each patient ranging from, 290mm to 400mm, 21 to 44 slices, and 6 or 7 mm respectively. The matrix size 256x256, the echo time (TE) = 88 ms and the repetition time (TR) = 5000 ms remained constant across patients. Axial fast spin echo images were also acquired using 2D fast spin echo (FSE) sequence with

fat saturation. The TR was between 3.95 s and 6.65 s, and the echo train length (ETL) was 9. Data were acquired twice with different TEs: a long TE (64 to 83 ms) and a short TE (9 to 12 ms). The sequence with long TE is sensitive to T_2 weighting, therefore producing T2-weighted images. The images with short TE are proton density weighted. These two set of images were used to create T2 maps. The matrix size was 256x256, reconstructed to 512x512 by zero-padding. The field-of-view (FOV), number of slices, and slice thickness were adapted for each patient, ranging between 120 and 320 mm, 31 to 45 slices, and 4 or 5 mm, respectively. Patient 8 with pleomorphic liposarcoma on the shoulder was excluded from this study, because the reconstruction diameter of the b = 800 s/mm^2 DW-MR images were inconsistent with that of the DW-MR images acquired with other b-values. Rigid registration with MIM was unable to correct for this discrepancy.

The tumour characteristics and MRI data collected for each patient is summarized in Table 3–1.

Table 3–1: Patients in the study

Patient number	Tumour location	Tumour site	Tumour grade	Tumour type	Myxoid/Non-myxoid	MRI data
P001	Superficial	Right shoulder	High	UPS	Non-myxoid	Not usable due to different TRs
P002	Superficial	Left upper arm	High	UPS	Non-myxoid	Not usable due to different TRs
P003	Deep intramuscular	Left leg	Low	Myxoid liposarcoma	Myxoid	completed for visit 1 and 2
P004	Suprafascial	Left groin	High	Leiomyosarcoma	Non-myxoid	completed for visit 1, 2 and 3
P005	Deep subfascial	Left thigh	High	Myxofibrosarcoma	Myxoid	completed for visit 1, 2 and 3
P006	Superficial	Left thigh	High	Myxoid/round cell liposarcoma	Myxoid	completed for visit 1, 2 and 3
P006	Superficial	Left thigh	High	Myxoid/round cell liposarcoma	Myxoid	completed for visit 1, 2 and 3
P007	Deep intramuscular	Left thigh	Low	Myxoid liposarcoma	Myxoid	completed for visit 1, 2 and 3
P008	Superficial	Right shoulder	High	Pleomorphic liposarcoma	Non-myxoid	not usable due to different reconstruction diameters
P009	Deep intramuscular	Left forearm	Low	Synovial sarcoma	Non-myxoid	completed for visit 1, 2 and 3
P0010	Suprafascial	Right chest wall	High	UPS	Non-myxoid	completed for visit 1, 2 and 3

3.2.3 Apparent Diffusion Coefficient (ADC) map

The ADC of each voxel can be quantified by Eq. 4.3 with a minimum of two b values [57].

$$\frac{S_j}{S_{0,j}} = exp(-b \times ADC_j) \tag{3.1}$$

where j represents the voxel index, S_j is the signal intensity at a given voxel with nonzero diffusion gradient b, $S_{0,j}$ is the signal intensity at a voxel without diffusion gradient, b is the gradient factor and ADC is the apparent diffusion coefficient.

A linear regression model was fitted to the logarithm of $S_j/S_{0,j}$ against increasing b-values, where its slope is the ADC value of the voxel. ADCs for each voxel were computed and compared with four combinations of b-values: b = 0, 100, 500, 800 s/mm^2, b = 100, 500, 800 s/mm^2, b = 100, 800 s/mm^2,and b = 500, 800 s/mm^2.

3.2.4 Data Analysis

Tumour contours were defined on axial T2-weighted images by an experienced physician using commercially available software (MIM software, Cleveland, United States). DW-MR images were registered onto axial T2-weighted images using the rigid registration function in MIM, to correct for motion and misalignment between images. The mean and the standard deviation (SD) of the ADCs inside the tumour contours were computed with in house programs written in MATLAB (The MathWorks Inc., Natick, MA, 2000). The data points in this chapter are presented as means ± SD or standard error of the mean (SEM) as indicated.

Histogram analysis was also performed to produce the following quantitative parameters: mean, standard deviation, median, mode, maximum, minimum, kurtosis, skewness, entropy and percentiles. Mean and standard deviation represent the average and dispersion of the histogram respectively. The median is a more representitive estimation of the average for skewed distributions. The mode represents the value with highest counts. Kurtosis and skewness reflect the shape and asymmetry of the probability distribution, respectively. A flatter peak has a negative kurtosis; a sharp peak has a positive kurtosis. The interpretation of skewness is demonstrated in Figure 3–1. A positively skewed histogram has an elongated tail on the right side of the mean. Similarly, a negatively skewed histogram has an elongated trial on the left side of the mean. The entropy represents a statistical measure of the irregularities in a histogram. Finally, a percentile represents the value below which a percentage of observations is calculated [58].

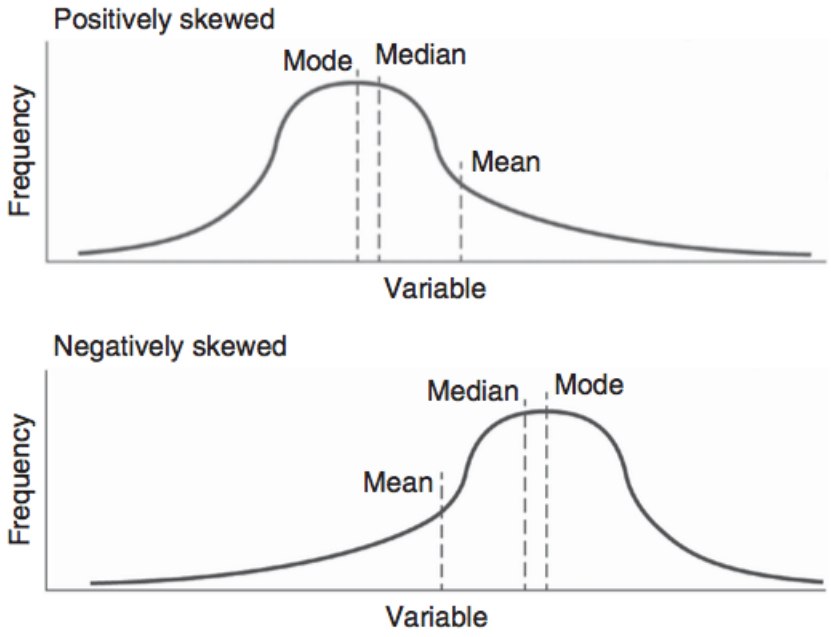

Figure 3–1: Interpretation of the skewness of histograms. This figure is adapted from [43]

3.2.5 Statistical Analysis

Differences among groups of data were assessed by one-way Analysis of Variance (ANOVA), followed by Tukey post-test, and accepted as statistically significant at $p < 0.05$. ANOVA provides information on whether there is a difference among groups of data. Tukey post-test, on the other hand, compares individual group to all the other groups. This gives us insights on which specific groups are significantly different.

3.3 Results and Discussions

3.3.1 ADC parametric map

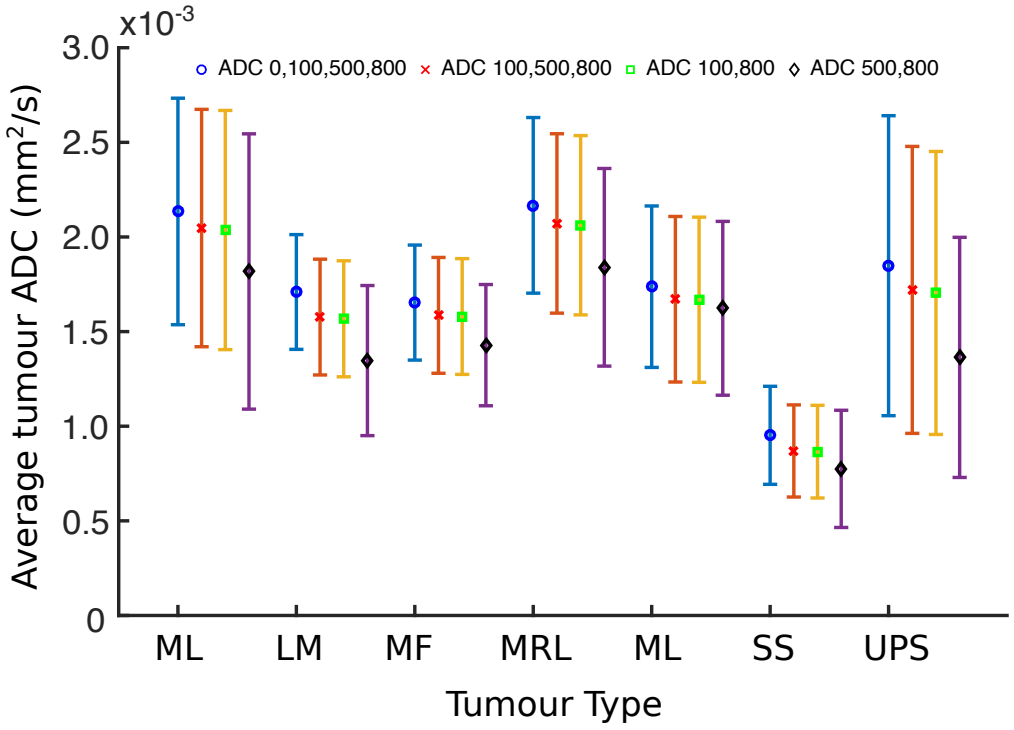

Figure 3–2: The volumetric mean ADCs computed using four combinations of b-values are plotted for each patient. Data points are mean ± standard deviation. The tumour type abbreviations ML, LM, MF, MRL, SS stand for myxoid liposarcoma, leimyosarcoma, myxofibrosarcoma, myxoid/round cell liposarcoma, and synovial sarcoma respectively.

$ADC_{0,100,500,800}$, $ADC_{100,500,800}$, $ADC_{100,800}$ and $ADC_{500,800}$ were computed for each tumour voxel with the combinations of b-values: b = 0, 100, 500, 800 s/mm^2,

b = 100, 500, 800 s/mm^2, b = 100, 800 s/mm^2,and b = 500, 800 s/mm^2, respectively. Depending on the choice of b-value combinations, the calculated volumetric mean ADCs are significantly different, as demonstrated in Figure 3–2. The mean $ADC_{0,100,500,800}$ is consistently greater than the mean $ADC_{100,500,800}$ and $ADC_{100,800}$ ($p < 0.001$), which is greater than the mean $ADC_{500,800}$ ($p < 0.001$) for each patient. $ADC_{100,500,800}$ and $ADC_{100,800}$ are not statistically different ($p > 0.05$).

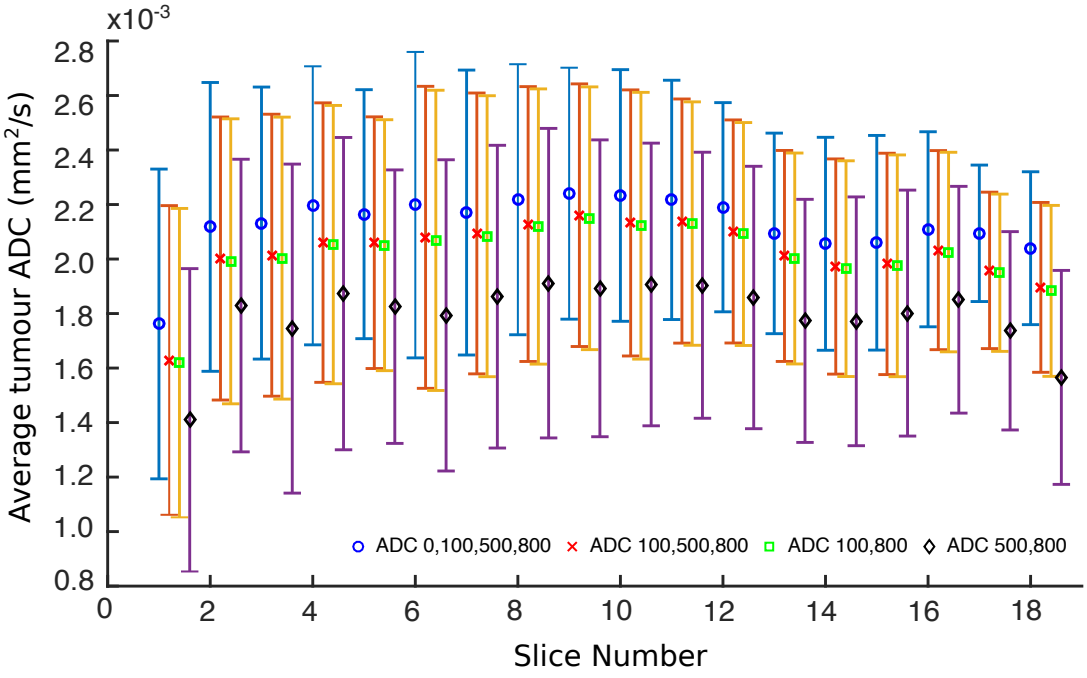

Figure 3–3: The mean ADCs computed using four combinations of b-values are plotted for individual slices of a patient with myxoid/round cell liposarcoma. Data points are mean ± standard deviation.

This behaviour found in volumetric mean ADCs is also observed on individual image slices. As an example, Figure 3–3 plots the mean tumour ADCs calculated

from each b-value combinations, for each image slice of a patient with myxoid liposarcoma. Again, the combination of b = 0, 100, 500, 800 s/mm^2 and b = 500, 800 s/mm^2 yield the highest and the lowest average ADCs ($p < 0.001$); the combination of b = 100, 500, 800 s/mm^2 and b = 100, 800 s/mm^2 return similar average ADCs ($p > 0.05$).

The discrepancy among the mean $ADC_{0,100,500,800}$, $ADC_{100,500,800}$, $ADC_{100,800}$ and $ADC_{500,800}$ is a result of the microcapillary perfusion detected at low b values. In 1989, Le Bihan et al has reported that the transformation between perfusion and true diffusion effect occurs at b-values in the 100-300 s/mm^2 range [59]. In order to capture the true diffusion effect, one should ideally use b-values greater than 300 s/mm^2 to compute the ADC maps. In our study, however, we have only acquired DW-MR images with two b-values greater than 300 s/mm^2. The decreased signal to noise ratio at high b-value DWIs causes increasing variations in the two-point estimation (b = 500 and 800 s/mm^2), thereby more error prone. This effect is captured by the increased standard deviation on the mean $ADC_{500,800}$ for 6 out of 7 patients, shown in Figure 3–2. Thus, for more reliable ADCs, the three-point estimation $ADC_{100,500,800}$ is used in the rest of this work. However, one should keep in mind that certain amount of perfusion could still be captured by $ADC_{100,500,800}$.

3.3.2 Pre-radiotherapy ADC analysis

Mean ADC value of myxoid and non-myxoid soft-tissue lesions

$ADC_{100,500,800}$ was computed for all seven malignant soft-tissue lesions. As a sanity check, the mean muscle ADC was also computed and compared against literature values. Muscle was selected because of its abundance in the extremities, where

soft-tissue sarcoma are mostly located. The mean muscle ADC is 0.001 ± 0.003 mm^2/s, consistent with literature reported ADC of 0.0011 ± 0.0001 [60]. However, the standard deviation from the measured mean muscle ADC is much larger than the literature reported value. One explanation could be that the contoured muscles are from various anatomical locations for each patient. The use of different imaging coils (extremity vs. body coil) could also increase the variation on the muscle ADC measurement.

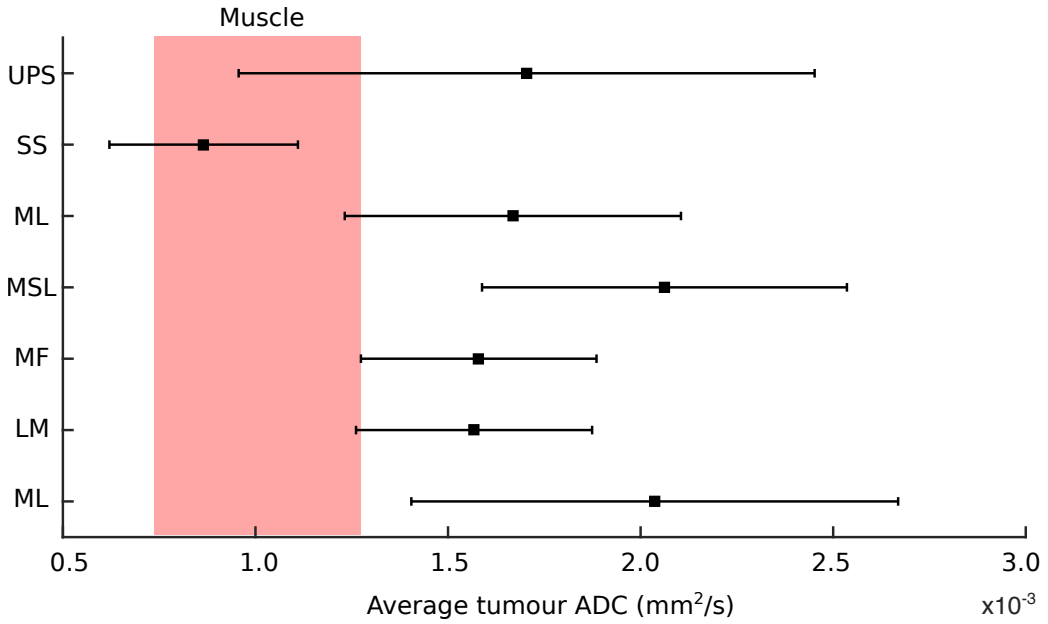

Figure 3–4: The mean ADCs ± standard deviation were plotted for each tumour. The pink rectangle represents the ADC range (within one standard deviation) of muscle, computed from muscle regions across all patients. The tumour type abbreviations ML, LM, MF, MRL, SS stand for myxoid liposarcoma, leimyosarcoma, myxofibrosarcoma, myxoid/round cell liposarcoma, and synovial sarcoma respectively.

The average tumour ADC ± SD of each tumour type is plotted in Figure 3–4. The large standard deviation reflects the heterogeneous compositions of these lesions. Notice that except for synovial sarcoma, all the other lesions have mean ADCs not only greater than that of muscle, but also much greater than 0.0011 mm^2/s. This observation contradicts the literature reported conclusion that malignant soft-tissue lesions should have ADCs smaller than $0.0011mm^2/s$ [60, 51, 61, 62]. As we looked for explanations, we realized that the ADC does not solely reflect the cellularity, but can also be influenced by the pathological composition of interstitial spaces. For example, myxoid matrix, an extracellular mucoid material with high water content has been reported to cause elevated ADCs [53]. Therefore, our initial hypothesis is that based on their ADCs, soft-tissue lesion can be categorized into non-myxoid containing lesions, such as synovial sarcoma, and myxoid-containing lesions.

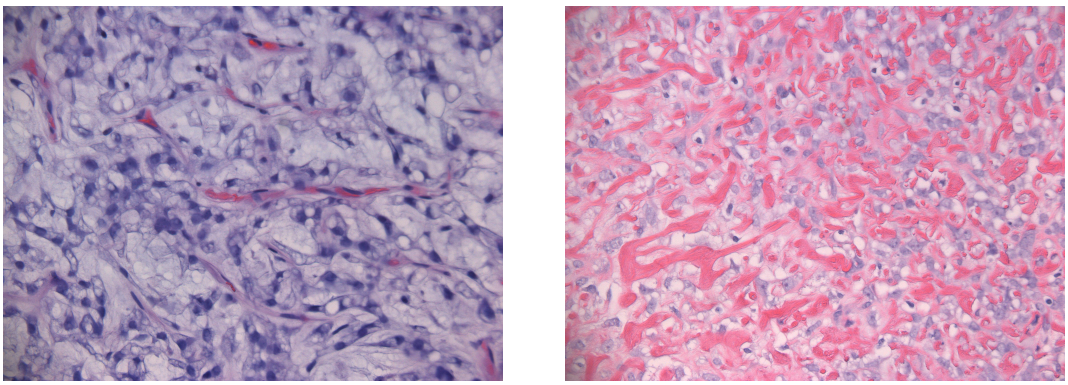

(a) (b)

Figure 3–5: (a) Photomicrograph of the histological specimen (hematoxylin-eosin stain) of myxoid liposarcoma (b) Photomicrograph of the histological specimen (hematoxylin-eosin stain) of synovial sarcoma. These images are provided by Dr. Sungmi Jung.

A histological specimen from each tumour was examined to verify this hypothesis. The histology clearly demonstrates two types of lesions: myxoid-containing lesions with abundant mucus-like myxoid matrix (Fig. 3–5(a)), and non-myxoid containing lesions with tightly packed cells (Fig. 3–5(b)). According to histology, our hypothesis is partially correct. Myxoid liposarcoma, myxoid/round cell liposarcoma and myxofibrosarcoma were confirmed as myxoid-containing lesions, whereas synovial sarcoma belongs to non-myxoid containing lesions. Nevertheless, there are two outliers to our hypothesis. Leiomyosarcoma and UPS, categorized as non-myxoid containing lesions based on histology, were both predicted as myxoid-containing lesions due to their high ADCs. Moreover, to our knowledge, no one has reported ADCs greater than $0.0011 mm^2/s$ from leiomyosarcoma or UPS. A possible explanation to this discrepancy could be that the histological specimen was only taken from a small section of each tumour, thereby can not represent the full tumour composition. However, the exact reason for their high ADCs remains unclear in this study.

ADC histogram analysis of myxoid and non-myxoid soft-tissue lesions

Table 3–2: Myxoid vs.Non-Myxoid

Tumour Type	ADC (mm^2/s)				
	Mean	Median	Kurtosis	Entropy	Skewness
Myxoid	0.0018 ± 0.0002	0.0019 ± 0.0003	3.6 ± 1.1	0.8 ± 0.2	-0.2 ± 0.5
Non-myxoid	0.0014 ± 0.0004	0.0013 ± 0.0004	4.1 ± 1.2	0.5 ± 0.5	0.6 ± 0.2
p-value	0.15	0.11	0.59	0.27	0.046

Based on tumour histology, the soft-tissue lesions in this study are divided into two categories: myxoid-containing lesions, including myxoid liposarcoma, myxoid/round cell liposarcoma and myxofibrosarcoma, and non-myxoid containing lesions including leiomyosarcoma, synovial sarcoma and UPS. The average mean, median, kurtosis, entropy and skewness of both groups are listed and compared in Table 3–2. The skewness successfully separates myxoid-containing tumours from non-myxoid containing tumours, with p-value of 0.046. All the other parameters are unable to differentiate these two groups.

Other observations

The mean, median, minimum, maximum, kurtosis, entropy, skewness and percentile of the ADC distribution from each lesion are also compared against tumour grade, tumour size and development of metastasis. However, no significant relationship was found.

3.3.3 Treatment evaluation

Diffusion weighted MR images were acquired before, 3 weeks and 8 weeks into the course of radiotherapy, which are referred to as pre-treatment, mid-treatment and post-treatment scans. The changes in ADC for the whole tumour are mapped out for each patient in this study. As an example, Figure 3–6(a) - (c) demonstrates the ADC maps of myxofibrosarcoma from these three time points. An overall increase in ADC subsequent to treatment is clearly observed. The histogram representation of the ADC distribution (Figure 3–6(d)) further confirms this observation. Post-surgical scans of this patient indicated no local reoccurrence or metastasis.

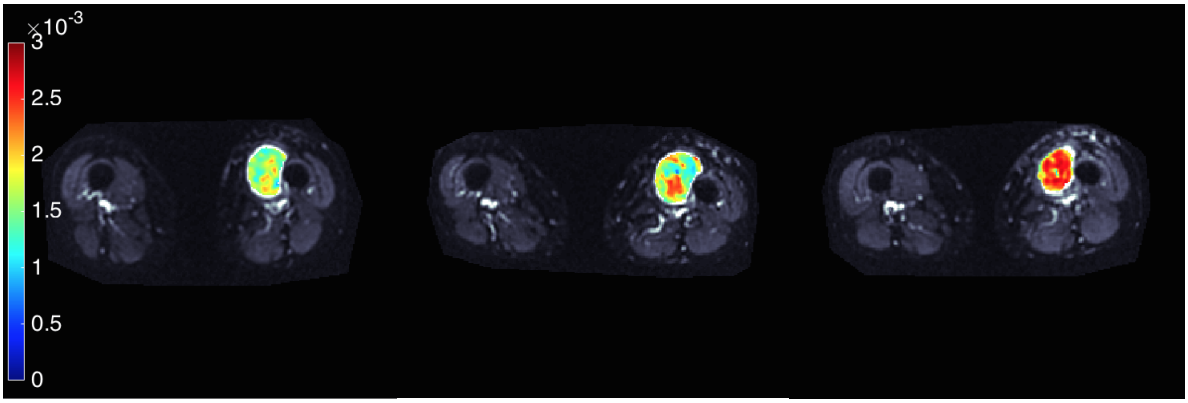

(a) (b) (c)

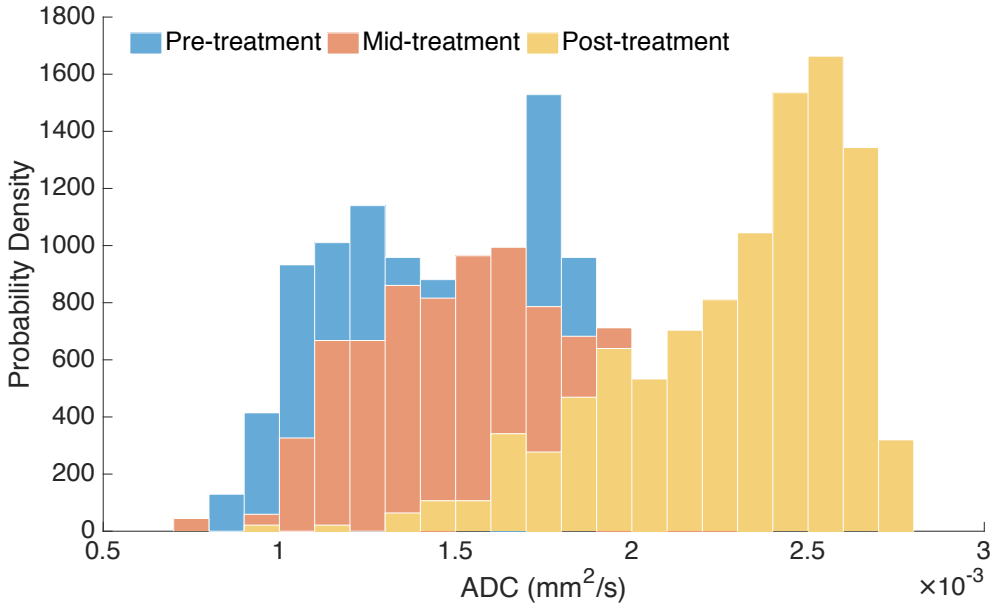

(d)

Figure 3–6: Example images from patient with Myxofibrosarcoma demonstrates increase in ADCs in (a) Pre-treatment (radiotherapy) ADC map (b) Mid-treatment ADC map and (c) Post-treatment ADC map. The therapy-induced increase in ADC is further illustrated with (d) Histogram representation of the ADC distribution at pre-treatment, mid- treatment and post-treatment.

The therapy-induced increase in ADC has been demonstrated in multiple literatures and is considered a sign for cell lysis and necrosis [26, 27, 28]. Before therapy, water movements are restricted by hydrophobic cellular membranes and by interactions with stromal structural proteins [63]. With successful therapy, mitotic catastrophe progresses to cell shrinkage and membrane blebbing (decoupling of the cytoskeleton from the plasma membrane) followed by necrosis formation and phagocytosis (removal of dead cells). Increased water movements, hence increased ADCs occur because of increased extracellular spaces, free water movements across cell membrane remnant and in the presence of necrosis. Since changes in ADC are usually seen before changes in tumour volume, increased ADC is considered as an early biomarker of successful therapy [63].

For other soft-tissue lesions in the study, the net mean $\pm$ standard error at pre-treatment, mid-treatment and post-treatment are used to illustrate the therapy induced changes in ADCs (Figure 3–7). Although all patients responded positively to radiotherapy and showed no local reoccurrence post-operations, three different progression trends are observed here. Myxoid liposarcoma (purple line), myxofibrosarcoma (orange line) and synovial sarcoma (green line) demonstrate continuous increasing in ADCs, as treatment progresses. Leiomyosarcoma (dark blue line) shows a slight decrease in ADCs at mid-treatment and elevated ADCs post-treatment. Finally, myxoid/round cell liposarcoma (yellow line) and UPS (light blue line) both have increased ADCs at mid-treatment, but decreased ADCs post-treatment.

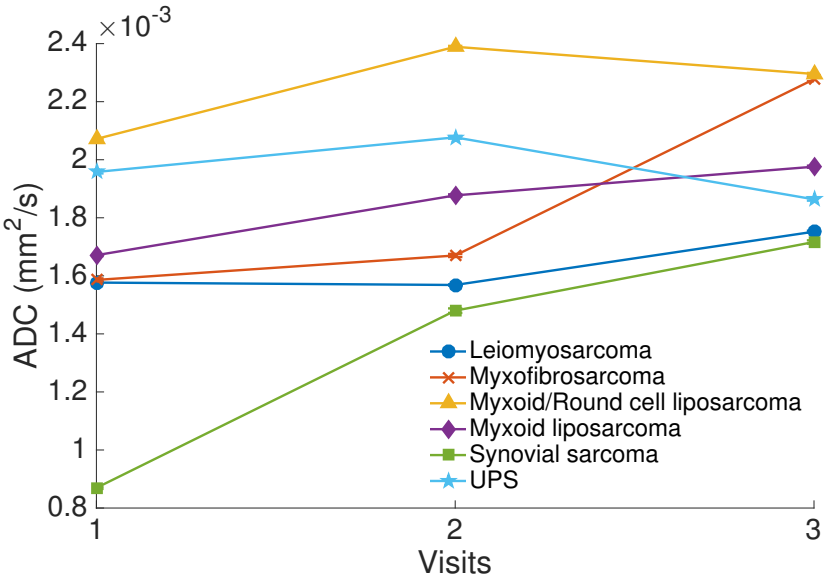

Figure 3–7: The mean ADCs ± standard error are plotted for each tumour at pre-treatment (visit 1), mid- treatment (visit 2) and post-treatment (visit 3).

These three progression trends correspond to three types of cell behaviour responding to radiotherapy. During therapy, cells may undergo apoptosis or cell lysis right away, exhibiting cell shrinkage, membrane blebbing or necrosis. A continuous increase in ADC would be observed in this case for reasons explained previously. In addition, cells can be resistant to therapy (no change in ADC values) or experience an initial transient cell swelling phase before apoptosis [64]. Cell swelling causes reduction in and increased tortuosity of the extracellular space, hence reduced ADC values. The initial ADC drop observed in leiomyosarcoma could be due to cell swelling. After therapy, removal of dead cells is followed by tissue compaction, fibrosis (the scaring of connective tissue) and regeneration of native tissues. Residual active disease or resistant cells can also repopulate themselves. Both activities

result in decreased ADC values. DW-MRI lacks the ability to distinguish fibrosis from residual active disease. Dynamic contrast enhanced MRI (DCE-MRI) and fluorodeoxyglucose positron emission tomography (FDG-PET) may be used to make the distinction. Reduced enhancement on DCE-MRI and low FDG uptake on PET is observed in the case of fibrosis, whereas residual active disease is associated with enhanced signal on DCE-MRI and high FDG uptake [63].

Lastly, our preliminary results indicate that the deep intramuscular tumours (N=3) consistently demonstrated a continuous increase of the mean ADCs during radiotherapy (Figure 3–8(a)), whereas superficial tumours (N=3) did not follow a specific trend (Figure 3–8(b)). The reason for this location dependent behaviour is unclear. Further investigation is needed to confirm this dependence and to explore its cause.

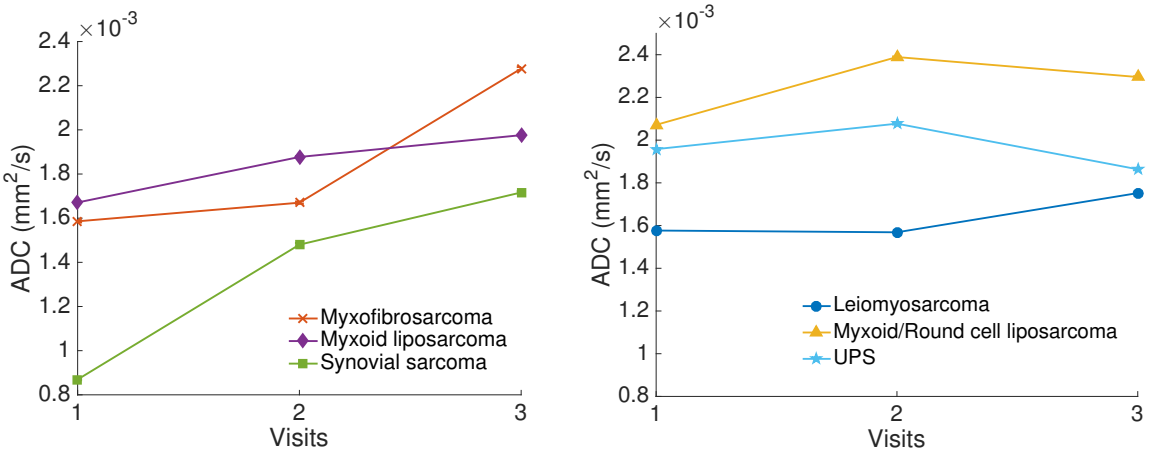

(a) (b)

Figure 3–8: The mean ADCs ± standard error are plotted for (a) deep intramuscular tumours and (b) superficial tumours.

3.3.4 Conclusion and further direction

Results of this preliminary study demonstrate that the pre-treatment mean tumor ADC can partially differentiate myxoid-containing and non-myxoid containing lesions, whereas skewness could act as a biomarker for this distinction. These high ADC values in myxoid-containing lesions are due to the presence of the myxoid matrix where free water is abundant in the extracellular spaces [53]. No significant relationship was found between the mean, median, minimum, maximum, kurtosis, entropy, skewness, percentile of the ADC distribution and tumour grade, tumour size or treatment outcome. The therapy induced change in ADC pre-, mid-, and post-treatment exhibit three distinct trends, corresponding to different cell behaviours in response to radiation: immediate apoptosis and necrosis, initial cell-swelling followed by apoptosis, and apoptosis followed by cell repopulation and fibrosis. All three trends mark successful treatment; all the patient in this study demonstrate no local reoccurrence after surgery. Finally, deep intramuscular tumours yield a consistent response to radiotherapy, unlike superficial tumours.

On the other hand, there are also limitations to this study. The major limitation is the small number of patients (N=8). At the time of this writing, more patients are being recruited to participate in this study. Additional data will be analyzed in the future to confirm our finding. The other challenge is to relate information obtained from MR images to histology, due to missing spatial information of the histological specimen. Image-guided biopsy could be considered in the future. Overall, the findings from this study show that DW-MRI and ADC measurements are a promising approach to soft-tissue sarcoma management.

CHAPTER 4
Automated segmentation of soft tissue sarcoma into distinct pathological regions using the apparent diffusion coefficient and T_2 relaxation

"Find beauty not only in the thing itself but in the pattern of the shadows, the light and dark which that thing provides." - Junichiro Tanizaki

4.1 Preface

The core of this thesis consists of one manuscript:

Shu Xing, Carolyn R. Freeman, Sungmi Jung and Ives R. Levesque. "Automated Segmentation of Soft Tissue Sarcoma Into Distinct Pathological Regions Using the Apparent Diffusion Coefficient and T_2 Relaxation", in preparation for submission to *Magnetic Resonance in Medicine*.

At the time of this writing, this manuscript is in preparation for submission to *Magnetic Resonance in Medicine*. The method section of this manuscript contains repetitive information from Chapter 3, because the same data set was used for both analyses.

4.2 Contribution of Authors

As the first author of this manuscript, I designed, implemented and validated all imaging methodology, performed the data analysis and drafted the paper. The contributions of the co-authors are listed as follows.

Carolyn R. Freeman, MD : recruited the soft-tissue sarcoma patients and provided tumour contours.

Sungmi Jung, MD : performed histological analysis of soft-tissue sarcoma lesions and provided the histological specimen photomicrographs.

Ives R. Levesque, PhD : As the candidate's supervisor, Dr. Levesque provided essential guidance and mentorship throughout the project, contributed to the data analysis of the T_2 maps and reviewed this manuscript.

Automated Segmentation of Soft Tissue Sarcoma Into Distinct Pathological Regions Using the Apparent Diffusion Coefficient and T_2 Relaxation

Shu Xing, MSc [1*], *Carolyn R. Freeman, MD* [2], *Sungmi Jung, MD* [3], *Ives R. Levesque, PhD* [1,4]

[1] Medical Physics Unit, McGill University, 845 Rue Sherbrook Ouest, Montreal, QC, Canada, H3A 0G4

[2] Radiation Oncology, McGill University Health Centre, 1001 Boul. Décarie, Montreal, QC, Canada H4A 3J1

[3] Department of Pathology, McGill University Health Centre, 1001 Boul. Décarie, Montreal, QC, Canada H4A 3J1

[4] Research Institute, McGill University Health Centre, 1001 Boul. Décarie, Montreal, QC, Canada H4A 3J1

In preparation for submission to Magnetic Resonance in Medicine

4.3 Abstract

Purpose: MRI is the imaging modality of choice for diagnosis and follow-up of soft-tissue sarcomas. Pathological tissue types within the tumor, such as high cellularity, high T2 content, or necrosis, can be interpreted with the combination of T2-weighted images, diffusion weighted (DW-MRI) and apparent diffusion coefficient (ADC) maps. This interpretation is important for diagnosis and evaluation of tumor heterogeneity. Conventionally, these tissue types are interpreted by visual inspection which can be time-consuming and subjective. In this work, we propose a novel method to automatically distinguish various pathological tissue types within a tumor.

Theory: To automate the tissue segmentation process, we chose the measured T2 value (T2 map) and the product of $exp(-\frac{TE}{T_2}) \cdot exp(-b \cdot ADC)$ (simDWI map) to represent the main physical characteristics captured by T2-weighted and DW-MRI respectively. Next, the trio of values (ADC, T2, simDWI) of each tumor voxel is compared against the average value from the reference muscle tissue. Each tumor voxel is assigned to a distinct pathological class according to the parameter values relative to the reference. Each class of tissue is represented by a different color.

Method: Axial DW-MRI and FSE images with fat saturation were acquired on a 1.5 T GE scanner in 5 patients with biopsy-confirmed sarcoma pre-, mid- and post-radiotherapy. Muscle regions were identified on the DW-MRI (b = 0 s/mm^2) for each patient. The reference mean and standard deviation ADC, T_2, and simDWI values were calculated including muscle voxels from all patients in the study.

Results: Based on the collective intensity patterns of the quantitative T_2, simDWI,

and ADC maps, regions of high T_2 content, high cellularity content, and necrosis were distinguished for various tumor types. The segmentation results are consistent with pathological observations from biopsy.

Conclusions: We successfully automated the process of differentiating radiologically significant tumor regions including high cellularity content, high T_2 content, necrosis, and fibrous tissues in soft tissue sarcoma.

Key words: diffusion-weighted imaging; soft-tissue sarcoma; tissue segmentation

4.4 Introduction

Magnetic resonance imaging (MRI), due to its excellent soft-tissue contrast, is the major imaging modalities for diagnosis, staging and follow-up of many soft-tissue tumours [65]. T_1 and T_2 relaxation characteristics obtained from conventional MRI sequences, such as fast spin-echo, allow the differentiation of abnormal lesions from normal tissues. Diffusion weighted MRI (DW-MRI) is an addition to the conventional MRI sequences for more accurate clinical diagnosis and cancer treatment evaluation. DW-MRI reveals information about the stochastic Brownian motion of water molecules on a microscopic level within tissues, which can be quantified by the apparent diffusion coefficient (ADC). It has been shown to differentiate benign and malignant lesions in the liver based on their apparent diffusion coefficient ADC, to aid diagnosis in gynaecological cancers, and to distinguish different components of brain tumours [66, 67, 68, 69]. In oncologic imaging, the biological premises for using DWI is that compared to benign or normal tissues, malignant tissues have higher cellularity, i.e. water diffusion is more restricted in malignant lesions [22]. Restricted water diffusion results in decreased signal loss and therefore increased signal intensity of malignant lesions on high b-value DW images, allowing for visual assessment. However, high b-value DW images also reflects the water content. Tissue that contains a large amount of water, such as massive liquefactive necrosis, causes increased signal intensity on high b-value images as well. In addition, water movement is a highly complex process and can also be affected by perfusion, tissue organization, extracellular space tortuosity and the integrity of cell membranes [65]. Therefore, to avoid misinterpretation, it is important to review DW images, ADC

maps and the morphological features from the associated conventional MR sequences in combination [65, 66, 63].

Several tissue types can be interpreted with the combination of T2-weighted, high b-value DW images and calculated ADC maps, as shown in Table 4–1, reproduced from Khoo et al, Koh et al and Patterson et al [65, 66, 63]. Tissue differentiation within the tumour can help physicians to accurately identify the malignant lesions. Conventionally, these tissue types are interpreted by visual inspection, which is time-consuming. In this work, we propose a novel method to automatically differentiate tissue types within the tumour, using normal muscle tissue as a reference.

Table 4–1: Interpretation of tumour tissues from diffusion-weighted images. This table is constructed based on [49, 51, 52].

Intensity of image on T2-weighted image	Intensity of image on high b-values DW-MRI (800 to 1000 s/mm^2)	Intensity of image on ADC	Interpretations
High	High	High	T2-shine through; often proteinaceous fluid
High-intermediate	High	Low	Tumour generally of high cellularity; rarely coagulative necrosis or abscess
High	Low	High	Fluid; liquefactive necrosis, lower cellularity; gland formation
Low-intermediate	Low	Low	Fibrous tissue with low water content with/without viable tumour cells

4.5 Theory

We start by considering how physicians visually differentiate tissue components within the tumour. The image intensity of the lesion is compared with some reference tissue in the background from the T2-weighted, high b-value DW images and the ADC maps, on a slice by slice basis. The image intensity pattern from these three images are then compare to the tissue type interpretation in Table 4–1. Notice that each voxel of T2-weighted and DW images contains the arbitrary MR signals, which depend on a number of factors, such as the type of sequence, imaging coils, field strength etc. The ADC map, on the other hand, is a parametric map that bears the value of the physical parameter (i.e. ADC) in each voxel. In order to automate the visual analysis process, we first bring these three images into a comparable space by quantifying the main physical parameters measured by T2-weighted and high b-value DW images.

4.5.1 Qualitative to Quantitative

T2-weighted image highlights differences in the T_2 relaxation time of tissues. Quantitative T_2 mapping is therefore an obvious choice to represent the physical characteristics captured by T2-weighted images.

Selecting a quantitative parameter to represent non-zero b-value DW images is more challenging. In the presence of paired magnetic field gradients, spins dephase and rephase proportional to the gradient lobe area of a diffusion weighted Echo Planar Imaging (EPI) sequence. At the echo time (TE), the loss of phase coherence in the transverse magnetization due to the spin-spin relaxation process produces a spin-echo amplitude attenuation, proportional to $exp(-TE/T_2)$. If a given voxel

contains moving spins during TE, an additional spin-echo amplitude attenuation is introduced due to further loss of phase coherence. This attenuation is due to the diffusion process and quantified as $exp(-b \cdot ADC)$. Overall, the signal for non-zero b-value DW images can be expressed as Equation. 4.1 [70].

$$S_{(b,TE)SE} = S_0 \cdot exp(-\frac{TE}{T_2}) \cdot exp(-b \cdot ADC) \tag{4.1}$$

where the signal at a given b-value is proportional to the signal amplitude S_0. S_0 includes contributions from proton density and incomplete T_1 relaxation effects, which is constant for a given voxel with negligible b and TE. The signal also depends on the echo time (TE), the spin-spin relaxation time (T_2), the diffusion-sensitizing gradient b and the ADC. It is obvious from this equation that the major physical characteristics are captured by the product of two exponential terms. For a given b-value, T_2 and ADC are the only two variables in this product, both reflecting the intrinsic property of tissue. Therefore, the dot product of these two exponentials, $exp(-\frac{TE}{T_2}) \cdot exp(-b \cdot ADC)$, is used to construct the surrogate map, or simulated DWI (simDWI), to represent the high b-value DW images.

Now, instead of interpreting tissue types from the combination of signal based T2-weighted and DW images along with ADC maps, as in Table 4–1, the quantitative maps of T_2, simDWI and ADC are used for tissue segmentation.

4.5.2 Reference Region Based Segmentation

In order to automate the previously mentioned visual analysis process, a reference tissue must be selected. Since soft tissue sarcoma is most commonly developed in the extremities where muscle is abundant, muscle was chosen to be the reference

tissue in this study. A global average of muscle from all patients is computed for T_2, simDWI and ADC maps, denoted as $\mu_{m,1}$, $\mu_{m,2}$, and $\mu_{m,3}$, respectively. This is under the premise that T_2 and ADC reflect the intrinsic properties of a given tissue, neglecting any artifactual effects of the imaging coil or magnetic field strength effect on T_2 and ADC measurements. For a given quantitative map, the value from each voxel in the tumour is then compared to the global average of the reference tissue following a two-step process. Figure 4–1 provides a simple schematic of this setup, where T and M denotes the tumour ROI and muscle ROI, and x_k represents the value of each tumour voxel.

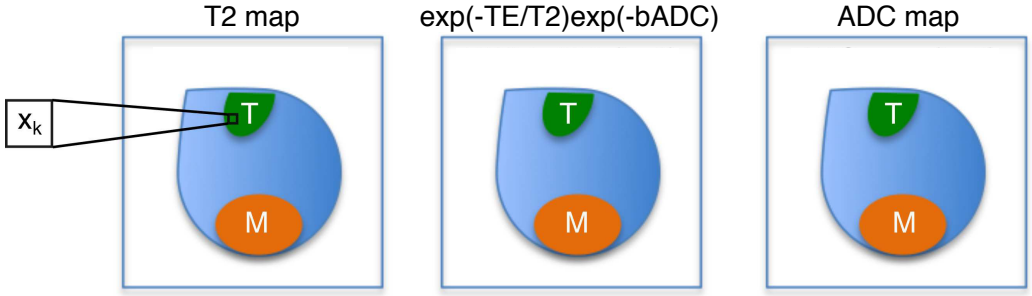

Figure 4–1: A schematic diagram of the T_2 map (k=1), the surrogate map of $exp(-\frac{TE}{T_2}) \cdot exp(-b \cdot ADC)$ (k=2) and ADC map (k=3). x represents the image intensity of each voxel in the tumour and k represents the type of quantitative map. x_k is compared against the global mean of the reference tissue, i.e. muscle (M), for each quantitative map. A binary decision is then made on which tissue type this voxel belongs to.

The combinatory relative intensities of tumour voxels with regards to muscle voxels from T_2, surrogate and ADC maps, yield four distinct combinations. Each combination is assigned to a different class of tissue, represented by a different colour. The tumour is then visualized by tissue types represented by different colours.

Step 1: A binary decision is made on which tissue type a voxel belongs to, according to the interpretation in Table 4–1. Each tissue type is represented by a different colour.

If $x_1 > \mu_{m,1}$, $x_2 > \mu_{m,2}$, $x_3 > \mu_{m,3}$, T2-shine through, assign voxel as red.

If $x_1 > \mu_{m,1}$, $x_2 > \mu_{m,2}$, $x_3 < \mu_{m,3}$, High cellularity tumour, assign voxel as green.

If $x_1 > \mu_{m,1}$, $x_2 < \mu_{m,2}$, $x_3 > \mu_{m,3}$, Necrosis, fluid, assign voxel as blue.

If $x_1 < \mu_{m,1}$, $x_2 < \mu_{m,2}$, $x_3 < \mu_{m,3}$, Fibrous tissue, assign voxel as grey.

Step 2: The degree of confidence that a voxel belongs to its corresponding tissue type correspond to the individual colour saturation, quantified by the square root of sum difference squared between x_k and $\mu_{m,k}$. A greater colour saturation indicates greater degree of confidence.

$$colour saturation = \sqrt{\sum_{k=1}^{3} (\frac{x_k - \mu_{m,k}}{\sigma_{m,k}})^2} \tag{4.2}$$

4.6 Methods

4.6.1 Patient

5 patients (3 females and 2 males; age range 48-81 years) were recruited with histological confirmed soft-tissue sarcoma to participate in this clinical study. All

tumours were malignant including one undifferentiated pleomorphic spindle cell sarcoma, one myxoid liposarcoma, one myxoid/round cell liposarcoma, one myxofibrosarcoma, and one synovial sarcoma. Lesions were located in the thigh(3), arm(1), and chest wall (1). Recruited patients satisfied the following criteria: (a) A biopsy must be down within 8 weeks prior to registration. (b) The tumour must be surgically resectable. (c) The patient must be fit for surgery. (d) The patient must be at least 18 years old. (e) For females with childbearing potential, a serum βHCG must be done 2 weeks prior to registration and the patient must practice adequate contraception. Patients with rhabdomyosarcoma, Ewing sarcoma, osteosarcoma and Kaposi sarcoma, metallic objects in the body, prior radiotherapy or excisional biopsy leading to the removal of the majority of the tumour were excluded from this study. The study was approved by the Research Ethics Board of the McGill University Health Center and written informed consent was obtained from each patient.

4.6.2 MRI Acquisition

Echo planar imaging (EPI) based DW-MR images were acquired with a 1.5 T MR scanner (GE Healthcare, Waukesha WI, USA) at b = 0, 100, 500, 800 s/mm^2 at three stages of the radiotherapy course: pre-(week 1), intra-(week 4) and post-radiotherapy (week 9). All 5 patients received surgery in week 10. The field-of-view, number of slices and slice thickness were adapted for each patient ranging from, 290mm to 400mm, 21 to 44 slices, and 6 or 7 mm respectively. The matrix size 256x256, the echo time (TE) = 88 ms and the repetition time (TR) = 5000 ms remained constant across patients. Axial fast spin echo images were also acquired using 2D fast spin echo (FSE) sequence with fat saturation. The TR was between

3.95 s and 6.65 s, and the echo train length (ETL) was 9. Data were acquired twice with different TEs: a long TE (64 to 83 ms) and a short TE (9 to 12 ms). The sequence with long TE is sensitive to T_2 weighting, therefore producing T2-weighted images. The images with short TE are proton density weighted. These two set of images were used to create T_2 maps. The matrix size was 256x256, reconstructed to 512x512 by zero-padding. The field-of-view (FOV), number of slices, and slice thickness were adapted for each patient, ranging between 120 and 320 mm, 31 to 45 slices, and 4 or 5 mm, respectively.

4.6.3 Data analysis

The ADC of each voxel can be quantified by Eq. 4.3 with a minimum of two b values [57].

$$\frac{S_j}{S_{0,j}} = exp(-b \times ADC_j) \tag{4.3}$$

where j represents the voxel index, S_j is the signal intensity at a given voxel with nonzero diffusion gradient b, $S_{0,j}$ is the signal intensity at a voxel without diffusion gradient, b is the gradient factor and ADC is the apparent diffusion coefficient.

Mapping of the apparent T_2 was performed by fitting a linear 2-parameter model to the logarithm of the FSE signal at every voxel (Eq. 4.4).

$$ln(S_j(TE_i)) = ln(S_{0,j}) - \frac{1}{T_{2,j}}(TE)_i \tag{4.4}$$

Where i = 1, 2 representing two different TEs, and j = voxel index. An example T2-weighted image acquired by the FSE sequence (long TE) and calculated T_2 map are shown in Figure 4–2.

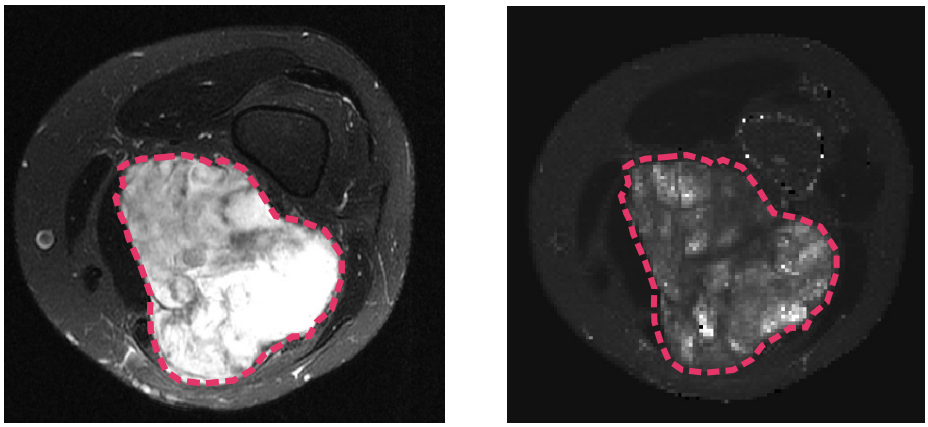

(a) (b)

Figure 4–2: (a) The axial T2-weighted images were acquired using 2D FSE with fat saturation. (b) T_2 map was computed with data collected at 2 different TEs: long TE selected by the scanner, and short TE. The lesion is contoured in red dotted lines.

Relative to muscle, the lesion is composed of high T_2 tissues. Fat should theoretically have lower T_2 values than muscle. However, due to the use of fat saturation in the imaging sequence, only the water hydrogen protons in the fat region are detected. Hence, the bright signal in the fat region observed from Figure 4–2 (a) and (b) reflects primarily the water hydrogen protons. It is important to acknowledge that some lipid-based protons still contributes to the T_2 relaxation of water protons through interaction effects, which can bias the T_2 measurement. Regions where fat saturation failed due to poor shimming were excluded from the fit, after visual inspection of the short TE data.

Tumour contours were defined on axial T2-weighted images by an experience physician using commercially available software (MIM software, Cleveland, United States). DW-MR images were registered onto axial T2-weighted images using the rigid registration function in MIM, to correct for motion and misalignment between images. The quantitative T_2, $exp(-\frac{TE}{T_2}) \cdot exp(-b \cdot ADC)$ and ADC maps were computed with in house programs written in MATLAB (The MathWorks Inc., Natick, MA).

Reference Tissue

Muscle regions of interest (ROIs) were identified on each slice using the DW b=0 s/mm^2 images (dotted lines in Fig.4–3(a)). These ROIs were then copied onto the quantitative T_2, simDWI and ADC maps. The total muscle voxels from all patients in this study for each map were plotted and fitted to a gaussian function, where their global means and standard deviations were computed. As an example, Fig. 4–3(b) demonstrates the ADC distribution of the muscle from all patients. The distribution appears to be gaussian with a R^2 of 0.987. The global mean and standard deviation were estimated from the fit to a gaussian function as 0.00101 $\pm$ 0.00003 mm^2/s and 0.000266 $\pm$ 0.00005 mm^2/s, respectively.

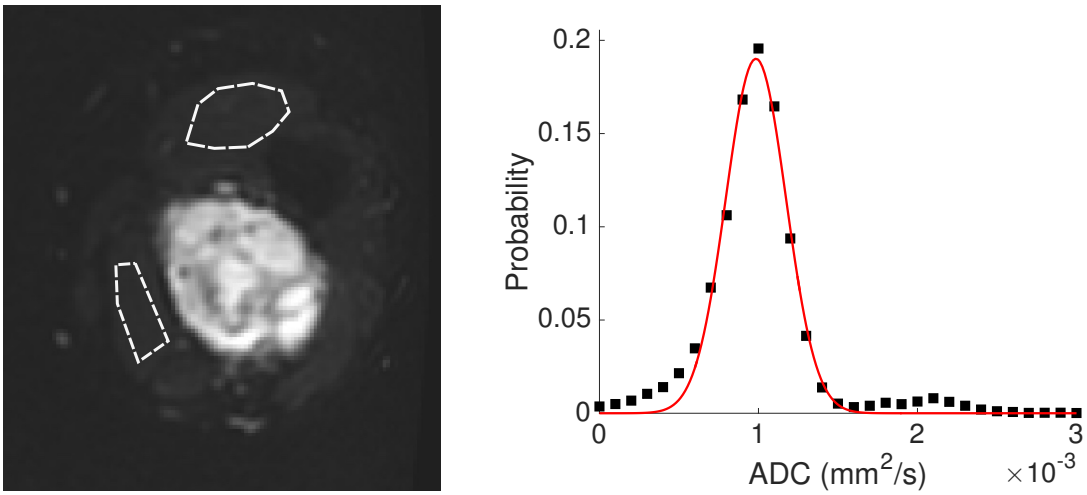

(a) (b)

Figure 4–3: Patient with myxoid liposarcoma. (a) Dotted lines mark the muscle ROIs, contoured on DW-MR images with b=0 s/mm^2. (b) A gaussian function G(x)=$a \cdot e^{(-(\frac{x-b}{c})^2}$ is fitted to the distribution of muscle ADCs from all patients, normalized to the total number of voxels (black squares). The red line represents the fitted curve. The ADC distribution of muscle appears to be gaussian with a R^2 of 0.987.

4.7 Results

The quantitative approach taken in the reference region based segmentation method is under the premise that T_2 and ADC reflect the intrinsic properties of a given tissue. We first validate this assumption by plotting the probability density function against the muscle ADC and T_2 measurements from each patient in Fig. 4–4(a) and Fig. 4–4(b) respectively.

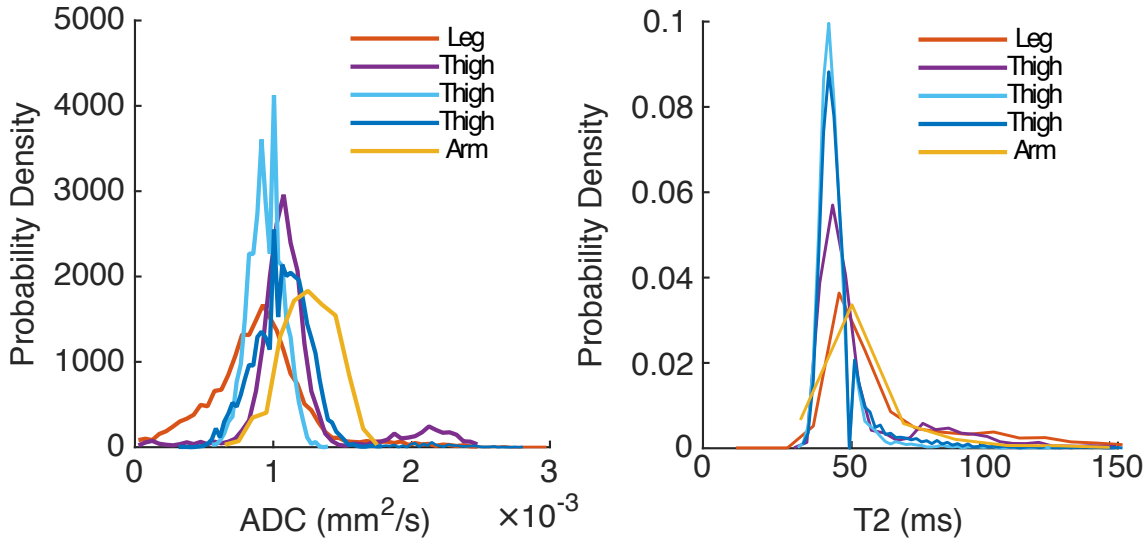

(a) (b)

Figure 4–4: (a) Probability distribution of muscle ADCs across patients yield a similar mean value. (b) Probability distribution of muscle T_2s across patients yield a similar mean value.

The mean muscle ADCs from each patient are centred around 0.001 mm^2/s, whereas the mean muscle T_2 are also centred around a common mean of 49 ms. This characteristic allows us to calculate a global mean and standard deviation for ADC and T_2 from muscle ROIs cross all patients, which during tissue segmentation are applied to images across all patients. The standard deviation of muscle ADCs and T_2s were computed as 0.0003 mm^2/s and 20 ms, respectively. Looking at the ADC and T_2 distributions more closely, we observe a slight anatomy dependence for both parameters. The mean muscle ADC and T_2 values from the arm are slightly higher than those from other anatomies.

4.7.1 Tissue Segmentation

In 5 patients who completed the imaging study at pre-, mid- and post-radiotherapy, all four types of tissues including high cellularity tumour, proteinaceous fluid, necrosis and fibrous tissue were identified within each lesion. Three sample pre-radiotherapy cases featuring proteinaceous fluid, high cellularity tumour and necrosis are discussed in detail here. Figure 4.7.1 illustrates the tissue segmentation of histology confirmed myxoid/round cell liposarcoma. As the name suggests, this type of lesion consists of loosely spaced myxoid extracellular matrix and densely packed round cells. Compared to muscle, the lesion exhibits higher intensities on T2-weighted (Figure 4.7.1 (a)), high b-value DW images (Figure 4.7.1(b)) and ADC maps (Figure 4.7.1 (c)). The combination of the quantitative T_2 (Figure 4.7.1 (d)), simDWI (Figure 4.7.1 (e)) and ADC map demonstrates the same "high (H)", "high (H)", "high (H)" pattern. According to Table 4–1, this pattern is interpreted as "T2-shine through" or proteinaceous fluid. The voxels with this pattern are assigned colour red with our proposed tissue segmentation method. In Figure 4.7.1 (f), we show that myxoid/round cell liposarcoma is predominately composed of high T_2 content, likely due to the extracellular myxoid matrix. The colour saturation indicates the degree of confidence that a given voxel belongs to this type. In this case, the brighter red regions are likely to be more myxoid rich than the darker red regions. The green regions in the middle of the tumour classify the high cellularity tumour, possibly the round cell portion. These observations are consistent with the histological findings shown in Fig. 4.7.1 (g) where clusters of round cells are located among large area of water abundant myxoid matrix. Parts of the lesion on the left lower edge are incorrectly classified

as necrotic tissue, represented by the colour blue. This originates from the bright band at the lower edge of the lesion on the ADC maps, which is an artifact due to imperfect rigid registration among DW images with different b-values.

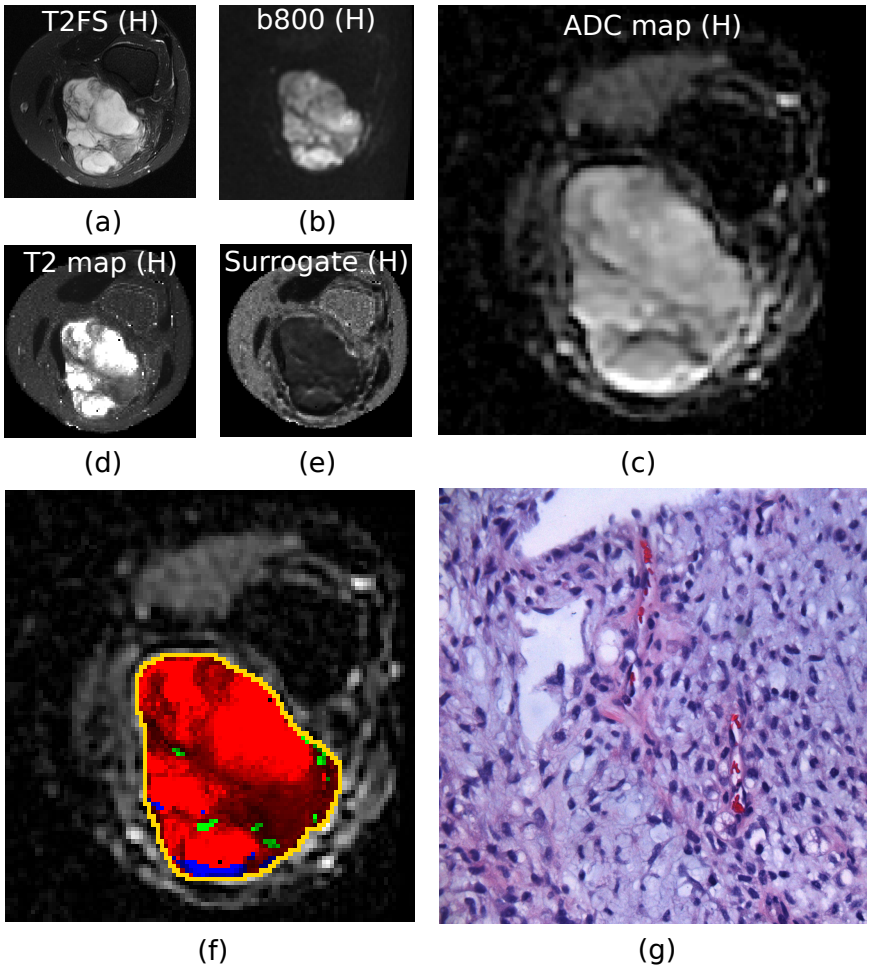

Figure 4–5: Patient with high grade myxoid/round cell liposarcoma in the left thigh. The lesion shows higher intensity (H) compare to the reference tissue in (a) Axial T2-weighted image acquired using 2D-FSE with fat saturation, (b) DW-MR image of one image slice acquired with with b = 800 s/mm^2, (c) ADC map calculated with b=100, 800 s/mm^2, (d) T_2 map and (e) Surrogate map constructed with $exp(-\frac{TE}{T_2}) \cdot exp(-b \cdot ADC)$. (f) This pattern is interpreted as T2-shine through or high T_2 content, correctly identified by the tissue segmentation method. high T_2 content is represented by colour red. The colour intensity is normalized to the mean intensity of each colour from the entire tumour. (e) Histological specimen shows lots of myxoid area with clusters of round cells.

The second type of tissue identified in Table 4–1 features high lesion intensity on T2-weighted and high b-value DW images, but low lesion intensity on the calculated ADC map. This "high (H)", "high (H)", "low (L)" pattern is commonly seen in malignant lesions, which results from increased cellularity and restricted diffusion [65]. Figure 4.7.1 demonstrates the tissue classification of synovial sarcoma, a malignant lesion with densely packed cells. The lesion appears to be bright on T2-weighted (Figure 4.7.1 (a)) and high b-value DW images (Figure 4.7.1 (b)). However, the ADC map (Figure 4.7.1 (c)) demonstrates low intensity within the lesion. This pattern is also observed on the combination of quantitative T_2 (Figure 4.7.1 (d)), simDWI (Figure 4.7.1 (e)) and ADC maps. Our segmentation method identifies the majority of the tumour as high cellularity malignant tissue, represented in green. Part of this lesion is classified as high T_2 content, shown in red. This observation is consistent with the histological findings shown in Figure 4.7.1 (g), where cells are closely spaced.

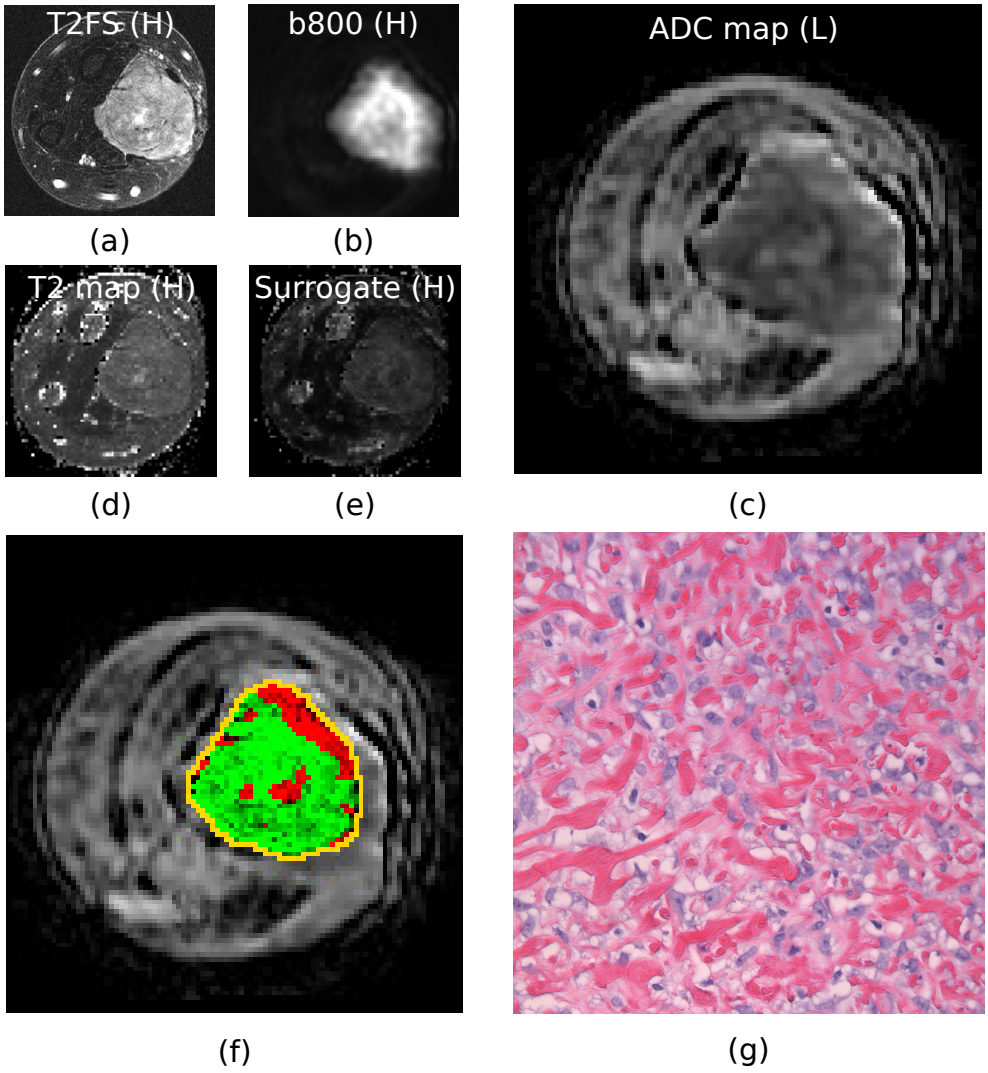

Figure 4–6: Patient with low grade synovial sarcoma on the forearm. The lesion shows higher intensity (H) compare to the reference tissue in (a) Axial T2-weighted image acquired using 2D-FSE with fat saturation, (b) DW-MR image of one image slice acquired with with b = 800 s/mm^2, (d) T_2 map, and (e) Surrogate map constructed with $exp(-\frac{TE}{T_2}) \cdot exp(-b \cdot ADC)$. The lesion demonstrates low intensity (L) on (c) ADC map calculated with b=100, 800 s/mm^2. (f) Tissue segmentation identifies abundant high cellularity tissue, represented in green. The colour intensity is normalized to the mean intensity of each colour from the entire tumour. (e) Histological specimen shows high cellularity.

A form of cell injury that results in the loss of membrane integrity, namely necrosis, is observed in a patient with undifferentiated pleomorphic spindle cell sarcoma (UPS) in the abdomen (Fig.4.7.1). In the necrotic regions, water experiences approximately unrestricted diffusion [71]. Necrotic tissue demonstrates high intensity on T2-weighted images (Figure 4.7.1 (a)) and has ADCs close to the value of free water (Figure 4.7.1 (c)), but low intensity on high b-value DW images (Figure 4.7.1 (b)). The combination of the quantitative T_2 (Figure 4.7.1 (d)), simDWI (Figure 4.7.1 (e)) and ADC map demonstrates "High (H)", "Low (L)", "High (H)" pattern. The voxels with such pattern are assigned the colour blue with our segmentation method. Figure 4.7.1 (f) illustrates the tissue segmentation of UPS, a highly dynamic soft-tissue lesion. Green regions representing high cellularity tumour and red regions representing high T_2 content are both observed in the lesion. The necrotic area is identified in blue. One could further confirm this by extracting a histological specimen from the necrotic area. Notice that there are black voxels in the necrotic region on the T_2 map. These are artifacts due to imperfect estimation of T_2. The black voxels in the segmentation map (Figure 4.7.1 (f)) are the result of these artifacts.

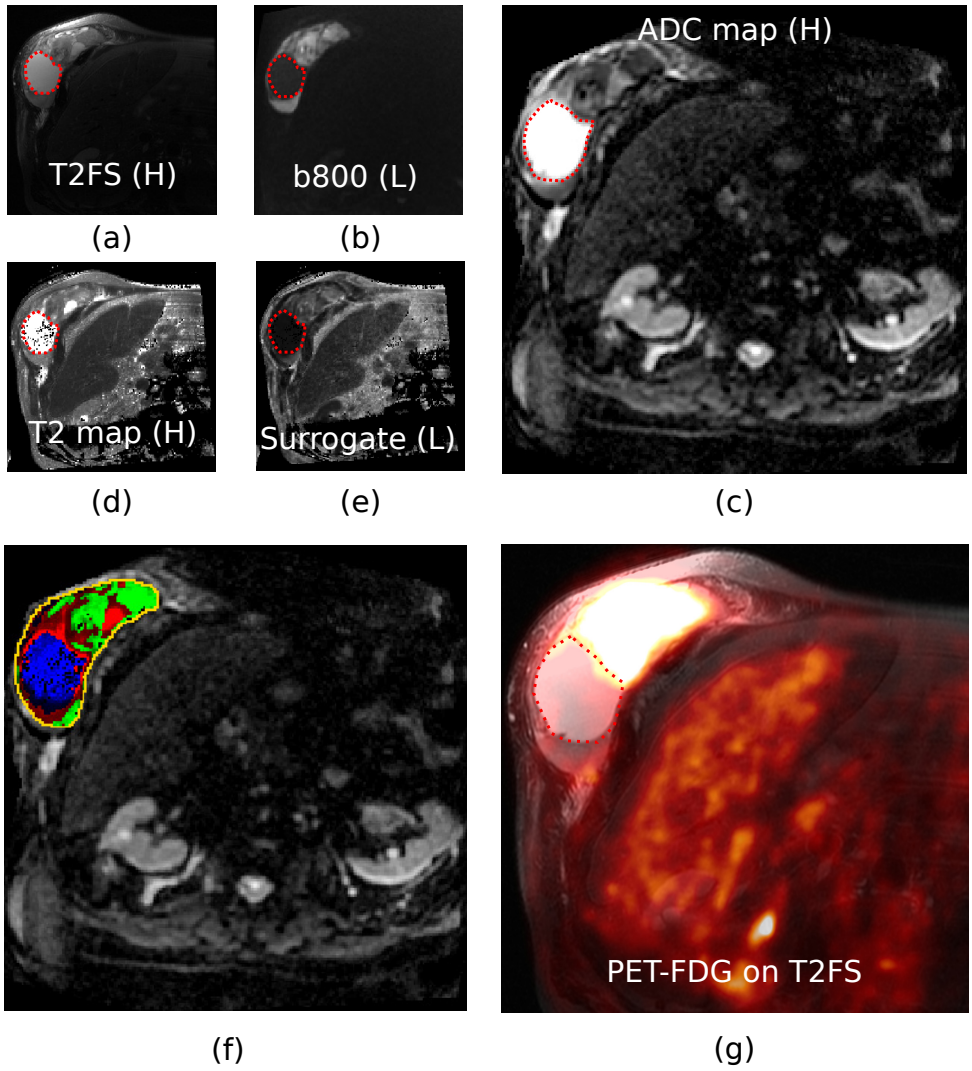

Figure 4–7: Patient with undifferentiated pleomorphic spindle cell sarcoma in the abdomen. The necrotic tissue (contoured in red dotted lines) shows higher intensity (H) compare to the reference tissue in (a) Axial T2-weighted image acquired using 2D-FSE with fat saturation, (c) ADC map calculated with b=100, 800 s/mm^2, and (d) T_2 map. The necrotic tissue demonstrates low intensity (L) on (b) DW-MR image of one image slice acquired with with b = 800 s/mm^2 and (e) simDWI. (f) Tissue segmentation shows the heterogeneity of the tumour. The colour intensity is normalized to the mean intensity of each colour from the entire tumour. The necrotic area in the tumour is coloured in blue.

With the reference region based segmentation method, we have successfully automated the tissue segmentation process to differentiate high T_2 content, high cellularity tumour, necrotic, and fibrous tissues for each patient at pre-, mid- and post-radiotherapy. The percentage composition of each tissue type, computed by dividing the total number of voxels from each category over the total number of tumour voxels, are summarized in Table 4–2.

Table 4–2: Tumor composition (% of the total tumour volume)

Tumor type	Time point	Red	Green	Blue	Grey	Artifact	Other
Myxofibrosarcoma	pre	96.6	2.4	0.6	0.00	0.4	0.00
	mid	97.0	1.2	0.9	0.0	0.8	0.1
	post	80.8	0.1	18.1	0.0	0.9	0.2
Myxoid/round cell liposarcoma	pre	90.0	1.7	8.0	0.0	0.3	0.0
	mid	82.4	2.4	13.4	0.0	1.6	0.2
	post	81.7	1.9	15.9	0.0	0.4	0.1
Myxoid liposarcoma	pre	93.1	5.7	0.8	0.0	0.1	0.3
	mid	74.0	4.9	16.8	0.1	0.3	3.9
	post	94.9	2.5	2.5	0.0	0.0	0.1
Synovial sarcoma	pre	24.0	73.8	0.7	0.1	0.5	0.9
	mid	74.8	8.3	16.1	0.1	0.1	0.6
	post	34.1	0.9	57.5	0.0	0.1	7.4
UPS	pre	61.6	13.0	19.3	0.0	5.9	0.2
	mid	66.8	6.7	20.3	0.0	6.0	0.2
	post	75.1	7.0	10.9	0.0	6.7	0.3

Columns labeled Red, Green, Blue and Grey represent high T_2 content, high cellularity tumour, necrotic tissue and fibrous tissues, respectively. The column labeled Artifact includes voxels with negative or zero ADC or T_2 values. These artifacts are due to noise or poor fitting during the generation of ADC and T_2 maps,

therefore does not reflect actual physical properties of tissue. The last column in this table contains the percentage voxels which exhibit a different pattern than the four tissue types included in our segmentation.

4.8 Discussion

The proposed reference region based segmentation successfully automated the tissue segmentation process. Based on the collective intensity patterns of the quantitative T_2, surrogate $exp(-\frac{TE}{T_2}) \cdot exp(-b \cdot ADC)$ and ADC maps, high T_2 content, high cellularity tissue, necrosis and fibrous tissues can be distinguished. We took an innovative approach in this method by designing a surrogate $exp(-\frac{TE}{T_2}) \cdot exp(-b \cdot ADC)$ map to replace the high b-value DW images. The product of two exponentials $exp(-\frac{TE}{T_2}) \cdot exp(-b \cdot ADC)$ carries the relative contribution from T_2 and ADC. Depending on the value of T_2 and ADC, either $exp(-\frac{TE}{T_2})$ or $exp(-b \cdot ADC)$ will become the major contributor to the surrogate image. When the lesion ADC and T_2 are both high relative to muscle, their weighted contribution plays a crucial role in distinguishing T2-shine through from necrosis. As water diffuses unrestrictedly in necrotic areas, necrotic tissues tend to have a much higher ADC than that of high T_2 content, but similar T_2 values. Therefore, while little change is observed in $exp(-\frac{TE}{T_2})$, $exp(-b \cdot ADC)$ decreases significantly for necrotic tissues, causing them to appear darker than muscle on the surrogate map.

The quantitative approach of using T_2, simDWI and ADC maps, instead of the signal based T2-weighted, high b-value DW image and ADC maps, has many advantages. Since T_2 and ADC reflect the intrinsic properties of a given tissue, a global mean and standard deviation of ADC and T_2 can be computed from muscle ROIs

cross all patients, which during tissue segmentation is applied to images without identifiable muscle. For instance, the UPS lesion shown in Figure 4.7.1 is located in the abdomen, where muscle regions are difficult to find. Our tissue segmentation method is still able to distinguish different tissue types within this lesion, by applying the global mean and standard deviation of ADC and T_2, computed from muscle regions in the other patients. Moreover, considering ADC and T_2 values are theoretically independent of coil loading or field strength, their global means and standard deviations can be used to perform tissue segmentation on future patients, therefore, muscle contouring will no longer be necessary.

The reference region based segmentation also has disadvantages. Its limitation lies in the imperfection of the T_2 and ADC measurements. As shown in Figure 4–4, the mean muscle ADC and T_2 values from the arm are slightly higher than that from other anatomies. In other words, the estimated global mean muscle ADC and T_2 are lower than the actual muscle means for this patient. This patient was diagnosed with synovial sarcoma in the forearm, illustrated in Figure 4.7.1. Our tissue segmentation method identified 74% of the lesion as high cellularity tumour along with 24% high T_2 content. If the actual muscle mean ADC and T_2 from the arm are used, 93% of the lesion is classified as high cellularity tumour. This discrepancy occurs in voxels whose ADC value is smaller than the actual mean muscle ADC in the arm, but greater than the global mean muscle ADC. Since the relative ADC intensity of lesion to muscle is the one separating high T_2 content from high cellularity tumour, the difference the mean muscle ADCs causes a different classification for these voxels. Now, the higher average muscle ADC and T_2 in the forearm could be due to its

inherent biological difference from the muscle in other anatomies. Yanagisawa et al. has reported different ADC values found in the skeletal muscles: the ankle dorsiflexor and the erector spinae muscles [72]. Another possible cause for the discrepancy in the mean muscle ADC and T_2 measurements is the choice of the receiving arrays. The forearm was imaged with a HD TR knee coil, whereas the other patients were imaged with a 8 channel body coil. Although the T_2 and ADC theoretically reflects the intrinsic properties of the tissue, in reality, the choice of receiving arrays and coil loading could still have artifactual effects on the estimation of these quantitative parameters. Further controlled experiments are needed to confirm the exact cause for the higher mean muscle ADC and T_2 in the forearm.

Table 4–2 summarized the percentage composition of each tissue type in the lesions at three stages of radiotherapy. At the pre-radiotherapy stage, the tumour percentage composition obtained from tissue segmentation easily separates myxoid-containing lesions from non-myxoid-containing lesions. All myxoid-containing lesions including myxofibrosarcoma, myxoid/round cell liposarcoma and myxoid liposarcoma have more than 90 % high T_2 content. On the other hand, the non-myxoid containing lesion, synovial sarcoma, only has 24.01 % high T_2 content. 73.77 % of the lesion is classified as high cellularity malignant tissue. UPS is a highly heterogeneous tumour, composed of 61.61% of high T_2 content, 13.03% of high cellularity malignant tissue and 19.31% of necrosis. We suspect that part of this lesion also contains myxoid matrix. However, further histological analysis is needed to confirm this hypothesis.

Post-radiotherapy effects can also be evaluated. Koh. et al reported that effective anticancer treatment results in tumour lysis, loss of cell membrane integrity, increased extracellular space and therefore an increase in water diffusion [73]. In 4 out of 5 patients in our study, the percentage of high cellularity malignant tissue consistently decreases from pre-, mid- to post-radiotherapy. Myxoid/round cell liposarcoma, however, demonstrates increased high cellularity malignant tissue, as treatment progresses. All the patients in this study exhibit no local reoccurrence, post-operation. Patient with myxoid/round cell liposarcoma developed lung metastasis 6 month after the surgery, whereas no lung metastasis were found in other patients. One might speculate that the increase in high cellularity tissue signifies poor treatment results, related to the development of metastasis. Nonetheless, more patients are needed to confirm this speculation.

Another indication of successful therapy is the formation of necrosis. With the exception of UPS, all the other lesions have greater percentage of necrotic tissue at post-radiotherapy than that at pre-radiotherapy. For myxoid liposarcoma and UPS, the necrotic percentage increased from pre- to mid-radiotherapy and decrease from mid- to post-radiotherapy. A possible explanation for this behaviour is that phagocytosis, tissue compaction and regeneration of native tissue could happen after necrosis formation. Hence, part of the necrotic tissues might be removed and replaced with connective tissues or native tissues.

4.9 Conclusion

In this work, we have successfully automated the process of differentiating high T_2 contents, high cellularity tumours, necrotic and fibrous tissues in the tumour.

Compare to background tissues, the image intensity of these four types of tissues in the lesion demonstrate distinct patterns on the T2-weighted, high b-value DW images and ADC maps as (High, High, High), (High, High, Low), (High, Low, High) and (Low, Low, Low) respectively. Since both T2-weighted and high b-value DW images are signal based, quantitative T_2 maps and simDWI map were generated to replace them. In other words, instead of interpreting tissue types from the combination of signal based T2-weighted and DW images along with ADC maps, the quantitative maps of T_2, simDWI and ADC are used in this study. Using muscle as a reference tissue, the reference region based segmentation was applied to the quantitative T_2, simDWI and ADC maps from 5 soft-tissue sarcoma patients at pre-, mid- and post-radiotherapy. The segmentation results at pre-radiotherapy stage are consistent with tumour histology. Radiotherapy induced effects were also assessed here. We found that in 4 out of 5 patients, high cellularity malignant tissue decreased as treatment progressed. An increasing percentage of necrosis was also observed with radiotherapy. The major limitation of this work is the small number of patients (N=5). More clinical data are needed to further evaluate this method.

CHAPTER 5
Conclusion

The topic of interest in this thesis is to use diffusion weighted MR imaging to evaluate therapy response and to better understand the microenvironment of soft tissue sarcoma. As part of a broad study, conventional T2-weighted and diffusion weighted images were acquired in patients with diagnosed soft-tissue sarcoma before, during and after pre-operative radiotherapy.

In this work, we have shown that the pre-treatment mean tumor ADC can partially differentiate myxoid-containing and non-myxoid containing lesions, whereas skewness could act as a biomarker for this distinction. These high ADC values in myxoid-containing lesions are due to the presence of the myxoid matrix where free water is abundant in the extracellular spaces [53]. No significant relationship was found between the mean, median, minimum, maximum, kurtosis, entropy, skewness, percentile of the ADC distribution and tumour grade, tumour size or treatment outcome. The therapy-induced change in ADC exhibit three distinct trends, corresponding to different cell behaviours in response to radiation: immediate apoptosis and necrosis, initial cell-swelling followed by apoptosis, and apoptosis followed by cell repopulation and fibrosis. All three trends mark successful treatment; all the patient in this study demonstrates no local reoccurrence after surgery. Finally, deep intramuscular tumours yield a consistent response to radiotherapy, unlike superficial tumours.

In the effort to better understand the tumour microenvironment, we proposed a reference region based segmentation method which successfully automated the process of differentiating high T_2 contents, high cellularity tumours, necrotic and fibrous tissues in the tumour. This method uses the combination of quantitative T_2 map, the surrogate $exp(-\frac{TE}{T_2}) \cdot exp(-b \cdot ADC)$ map and ADC map. Each voxel intensity in the lesion is compared against the average intensity of the reference tissue for all three maps. Their combinatory pattern yield four distinct combinations. Each combination is assigned to a different tissue class, represented by a different colour. Using muscle as a reference tissue, the reference region based segmentation was applied to 5 soft-tissue sarcoma patients at pre-, mid- and post-radiotherapy. The segmentation results at pre-radiotherapy stage are consistent with tumour histology. Radiotherapy induced effects were also assessed here. We found that in 4 out of 5 patients, high cellularity malignant tissue decreased as treatment progressed. An increasing percentage of necrosis was also observed with radiotherapy.

The major limitation in this study is the small number of patients. A total of 10 patients were recruited for this study. Usable MR images acquired at pre-radiotherapy were available for 8 out of 10 patients. Only 5 out of 10 patients have completed the study at pre-, mid- and post-radiotherapy. At the time of writing, more patients are being recruited to participate in this study. The data will be analyzed to confirm our findings. The other challenge is to relate information obtained from MR images to histology, due to missing spatial information of the histological specimen. Image-guided biopsy could be considered in the future. Nevertheless, we

have shown that diffusion weighted MRI is a valuable tool for understanding the microenvironment of soft tissue sarcoma and the evaluation of treatment response.

References

[1] Tal Geva. Magnetic resonance imaging: historical perspective. *Journal of Cardiovascular Magnetic Resonance*, 8(4):573–580, 2006.

[2] R Damadian, M Goldsmith, and L Minkoff. Nmr in cancer: Xvi. fonar image of the live human body. *Physiological chemistry and physics*, 9(1):97–100, 1976.

[3] EO Stejskal and JE Tanner. Spin diffusion measurements: spin echoes in the presence of a time-dependent field gradient. *The journal of chemical physics*, 42(1):288–292, 1965.

[4] Susumu Mori and Peter B Barker. Diffusion magnetic resonance imaging: its principle and applications. *The Anatomical Record*, 257(3):102–109, 1999.

[5] ME Moseley, J Kucharczyk, J Mintorovitch, Y Cohen, J Kurhanewicz, N Derugin, H Asgari, and D Norman. Diffusion-weighted mr imaging of acute stroke: correlation with t2-weighted and magnetic susceptibility-enhanced mr imaging in cats. *American Journal of Neuroradiology*, 11(3):423–429, 1990.

[6] Michael E Moseley, Yoram Cohen, J Kucharczyk, J Mintorovitch, HS Asgari, MF Wendland, J Tsuruda, and D Norman. Diffusion-weighted mr imaging of anisotropic water diffusion in cat central nervous system. *Radiology*, 176(2):439–445, 1990.

[7] Thomas L Chenevert, James A Brunberg, and JG Pipe. Anisotropic diffusion in human white matter: demonstration with mr techniques in vivo. *Radiology*, 177(2):401–405, 1990.

[8] Robert W Brown, Y-C Norman Cheng, E Mark Haacke, Michael R Thompson, and Ramesh Venkatesan. *Magnetic resonance imaging: physical principles and sequence design*. John Wiley & Sons, 2014.

[9] Dwight G Nishimura. *Principles of magnetic resonance imaging*. Standford Univ., 2010.

[10] Paul Davies. *The new physics*. Cambridge University Press, 1992.

[11] Catherine Westbrook and Carolyn Kaut Roth. *MRI in Practice*. John Wiley & Sons, 2011.

[12] Edward Conrad Jordan and Keith G Balmain. *Electromagnetic waves and radiating systems*, volume 4. Prentice-Hall Englewood Cliffs, NJ, 1968.

[13] Donald W McRobbie, Elizabeth A Moore, Martin J Graves, and Martin R Prince. *MRI from Picture to Proton*. Cambridge university press, 2006.

[14] A Einstein. Un the movement of small particles suspended in statiunary liquids required by the molecular-kinetic theory 0f heat. 1905.

[15] Denis Le Bihan and E Breton. Imagerie de diffusion in-vivo par résonance magnétique nucléaire. *Comptes-Rendus de l'Académie des Sciences*, 93(5):27–34, 1985.

[16] ME Moseley, Y Cohen, J Mintorovitch, L Chileuitt, H Shimizu, J Kucharczyk, MF Wendland, and PR Weinstein. Early detection of regional cerebral ischemia in cats: comparison of diffusion-and t2-weighted mri and spectroscopy. *Magnetic resonance in medicine*, 14(2):330–346, 1990.

[17] Denis Le Bihan, Eric Breton, Denis Lallemand, ML Aubin, J Vignaud, and M Laval-Jeantet. Separation of diffusion and perfusion in intravoxel incoherent motion mr imaging. *Radiology*, 168(2):497–505, 1988.

[18] HL Lutsep, GW Albers, A DeCrespigny, GN Kamat, MP Marks, and ME Moseley. Clinical utility of diffusion-weighted magnetic resonance imaging in the assessment of ischemic stroke. *Annals of neurology*, 41(5):574–580, 1997.

[19] Yaniv Assaf and Ofer Pasternak. Diffusion tensor imaging (dti)-based white matter mapping in brain research: a review. *Journal of molecular neuroscience*, 34(1):51–61, 2008.

[20] Patric Hagmann, J-P Thiran, Lisa Jonasson, P Vandergheynst, S Clarke, P Maeder, and Reto Meuli. Dti mapping of human brain connectivity: statistical fibre tracking and virtual dissection. *Neuroimage*, 19(3):545–554, 2003.

[21] DJ Werring, CA Clark, GJ Barker, AJ Thompson, and DH Miller. Diffusion tensor imaging of lesions and normal-appearing white matter in multiple sclerosis. *Neurology*, 52(8):1626–1626, 1999.

[22] Anwar R Padhani, Guoying Liu, Dow Mu-Koh, Thomas L Chenevert, Harriet C Thoeny, Taro Takahara, Andrew Dzik-Jurasz, Brian D Ross, Marc Van Cauteren, David Collins, et al. Diffusion-weighted magnetic resonance imaging as a cancer biomarker: consensus and recommendations. *Neoplasia*, 11(2):102–125, 2009.

[23] Yong Guo, You-Quan Cai, Zu-Long Cai, Yuan-Gui Gao, Ning-Yu An, Lin Ma, Srikanth Mahankali, and Jia-Hong Gao. Differentiation of clinically benign and malignant breast lesions using diffusion-weighted imaging. *Journal of magnetic resonance imaging*, 16(2):172–178, 2002.

[24] Shantanu Sinha, Flora Anne Lucas-Quesada, Usha Sinha, Nanette DeBruhl, and Lawrence W Bassett. In vivo diffusion-weighted mri of the breast: Potential for lesion characterization. *Journal of magnetic resonance imaging*, 15(6):693–704, 2002.

[25] Xi-Jie Sun, Xian-Yue Quan, Fan-Heng Huang, and Yi-Kai Xu. Quantitative evaluation of diffusion-weighted magnetic resonance imaging of focal hepatic lesions. *World journal of gastroenterology: WJG*, 11(41):6535–6537, 2005.

[26] Rebecca J Theilmann, Rebecca Borders, Theodore P Trouard, Guowei Xia, Eric Outwater, James Ranger-Moore, Robert J Gillies, and Alison Stopeck. Changes in water mobility measured by diffusion mri predict response of metastatic breast cancer to chemotherapy. *Neoplasia*, 6(6):831–837, 2004.

[27] Chiao-Yun Chen, Chun-Wei Li, Yu-Ting Kuo, Twei-Shiun Jaw, Ding-Kwo Wu, Jo-Chi Jao, Jui-Sheng Hsu, and Gin-Chung Liu. Early response of hepatocellular carcinoma to transcatheter arterial chemoembolization: choline levels and mr diffusion constants?initial experience 1. *Radiology*, 239(2):448–456, 2006.

[28] Shinji Naganawa, Chiho Sato, Hisashi Kumada, Takeo Ishigaki, Shunichi Miura, and Osamu Takizawa. Apparent diffusion coefficient in cervical cancer of the uterus: comparison with the normal uterine cervix. *European radiology*, 15(1):71–78, 2005.

[29] Sara Leibfarth, Franziska Eckert, Stefan Welz, Christine Siegel, Holger Schmidt, Nina Schwenzer, Daniel Zips, and Daniela Thorwarth. Automatic delineation of tumor volumes by co-segmentation of combined pet/mr data. *Physics in medicine and biology*, 60(14):5399, 2015.

[30] Stefan Bauer, Roland Wiest, Lutz-P Nolte, and Mauricio Reyes. A survey of mri-based medical image analysis for brain tumor studies. *Physics in medicine and biology*, 58(13):R97, 2013.

[31] Sahar Ghanavati, Junning Li, Ting Liu, Paul S Babyn, Wendy Doda, and George Lampropoulos. Automatic brain tumor detection in magnetic resonance images. In *Biomedical Imaging (ISBI), 2012 9th IEEE International Symposium on*, pages 574–577. IEEE, 2012.

[32] Ahmet Ekin. Pathology-robustmr intensity normalizationwith global and local constraints. In *Biomedical Imaging: From Nano to Macro, 2011 IEEE International Symposium on*, pages 333–336. IEEE, 2011.

[33] John G Sled, Alex P Zijdenbos, and Alan C Evans. A nonparametric method for automatic correction of intensity nonuniformity in mri data. *Medical Imaging, IEEE Transactions on*, 17(1):87–97, 1998.

[34] Idanis Diaz, Pierre Boulanger, Russell Greiner, and Albert Murtha. A critical review of the effects of de-noising algorithms on mri brain tumor segmentation. In *Engineering in Medicine and Biology Society, EMBC, 2011 Annual International Conference of the IEEE*, pages 3934–3937. IEEE, 2011.

[35] Alexander V Tuzikov, Olivier Colliot, and Isabelle Bloch. Evaluation of the symmetry plane in 3d mr brain images. *Pattern Recognition Letters*, 24(14):2219–2233, 2003.

[36] Lothar R Schad, Stefan Blüml, and Ivan Zuna. Ix. mr tissue characterization of intracranial tumors by means of texture analysis. *Magnetic resonance imaging*, 11(6):889–896, 1993.

[37] Shijun Wang and Ronald M Summers. Machine learning and radiology. *Medical image analysis*, 16(5):933–951, 2012.

[38] WE Phillips, RP Velthuizen, S Phuphanich, LO Hall, LP Clarke, and ML Silbiger. Application of fuzzy c-means segmentation technique for tissue differentiation in mr images of a hemorrhagic glioblastoma multiforme. *Magnetic resonance imaging*, 13(2):277–290, 1995.

[39] Hongmin Cai, Ragini Verma, Yangming Ou, Seung-koo Lee, Elias R Melhem, and Christos Davatzikos. Probabilistic segmentation of brain tumors based on multi-modality magnetic resonance images. In *Biomedical Imaging: From Nano*

to Macro, 2007. ISBI 2007. 4th IEEE International Symposium on, pages 600–603. IEEE, 2007.

[40] Rangaraj M Rangayyan, Fabio J Ayres, and JE Leo Desautels. A review of computer-aided diagnosis of breast cancer: Toward the detection of subtle signs. *Journal of the Franklin Institute*, 344(3):312–348, 2007.

[41] Stefan Klein, Uulke A van der Heide, Irene M Lips, Marco van Vulpen, Marius Staring, and Josien PW Pluim. Automatic segmentation of the prostate in 3d mr images by atlas matching using localized mutual information. *Medical physics*, 35(4):1407–1417, 2008.

[42] Mark J Kransdorf and Mark D Murphey. *Imaging of soft tissue tumors*. Lippincott williams & wilkins, 2006.

[43] PHA Nijhuis, M Schaapveld, R Otter, WM Molenaar, WTA Van Der Graaf, and HJ Hoekstra. Epidemiological aspects of soft tissue sarcomas (sts)?consequences for the design of clinical sts trials. *European Journal of Cancer*, 35(12):1705–1710, 1999.

[44] Christopher DM Fletcher, K Krishnan Unni, and Fredrik Mertens. *Pathology and genetics of tumours of soft tissue and bone*, volume 4. Iarc, 2002.

[45] Matthias R Benz, Johannes Czernin, Martin S Allen-Auerbach, William D Tap, Sarah M Dry, David Elashoff, Kira Chow, Vladimir Evilevitch, Jeff J Eckardt, Michael E Phelps, et al. Fdg-pet/ct imaging predicts histopathologic treatment responses after the initial cycle of neoadjuvant chemotherapy in high-grade soft-tissue sarcomas. *Clinical cancer research*, 15(8):2856–2863, 2009.

[46] Jim S Wu and Mary G Hochman. Soft-tissue tumors and tumorlike lesions: A systematic imaging approach 1. *Radiology*, 253(2):297–316, 2009.

[47] Steven A Rosenberg and Eli J Glatstein. Perspectives on the role of surgery and radiation therapy in the treatment of soft tissue sarcomas of the extremities. In *Seminars in oncology*, volume 8, page 190, 1981.

[48] MH Shiu, El B Castro, STEVEN I Hajdu, and JOSEPH G Fortner. Surgical treatment of 297 soft tissue sarcomas of the lower extremity. *Annals of surgery*, 182(5):597, 1975.

[49] STEVEN A Rosenberg, JOEL Tepper, E Glatstein, JOSE Costa, ALAN Baker, MURRAY Brennan, ERNEST V DeMoss, CLAUDIA Seipp, WILLIAM F Sindelar, PAUL Sugarbaker, et al. The treatment of soft-tissue sarcomas of the extremities: prospective randomized evaluations of (1) limb-sparing surgery plus radiation therapy compared with amputation and (2) the role of adjuvant chemotherapy. *Annals of surgery*, 196(3):305, 1982.

[50] Ellen Kapiteijn, Corrie AM Marijnen, Iris D Nagtegaal, Hein Putter, Willem H Steup, Theo Wiggers, Harm JT Rutten, Lars Pahlman, Bengt Glimelius, J Han JM van Krieken, et al. Preoperative radiotherapy combined with total mesorectal excision for resectable rectal cancer. *New England Journal of Medicine*, 345(9):638–646, 2001.

[51] So-Yeon Lee, Won-Hee Jee, Joon-Yong Jung, Michael Y Park, Sun-Ki Kim, Chan-Kwon Jung, and Yang-Guk Chung. Differentiation of malignant from benign soft tissue tumours: use of additive qualitative and quantitative diffusion-weighted mr imaging to standard mr imaging at 3.0 t. *European radiology*, pages 1–12, 2015.

[52] Pedro Augusto Gondim Teixeira, Frederique Gay, Bailiang Chen, Marie Zins, François Sirveaux, Jacques Felblinger, and Alain Blum. Diffusion-weighted magnetic resonance imaging for the initial characterization of non-fatty soft tissue tumors: correlation between t2 signal intensity and adc values. *Skeletal radiology*, pages 1–9, 2015.

[53] Masayuki Maeda, Akihiko Matsumine, Hiroya Kato, Katsuyuki Kusuzaki, Stephan E Maier, Atsumasa Uchida, and Kan Takeda. Soft-tissue tumors evaluated by line-scan diffusion-weighted imaging: Influence of myxoid matrix on the apparent diffusion coefficient. *Journal of Magnetic Resonance Imaging*, 25(6):1199–1204, 2007.

[54] Dirk Schnapauff, Martin Zeile, Manuel Ben Niederhagen, Barbara Fleige, Per-Ulf Tunn, Bernd Hamm, and Oliver Dudeck. Diffusion-weighted echo-planar magnetic resonance imaging for the assessment of tumor cellularity in patients with soft-tissue sarcomas. *Journal of Magnetic Resonance Imaging*, 29(6):1355–1359, 2009.

[55] Oliver Dudeck, Martin Zeile, Daniel Pink, Maciej Pech, Per-Ulf Tunn, Peter Reichardt, Wolf-Dieter Ludwig, and Bernd Hamm. Diffusion-weighted magnetic resonance imaging allows monitoring of anticancer treatment effects in patients

with soft-tissue sarcomas. *Journal of Magnetic Resonance Imaging*, 27(5):1109–1113, 2008.

[56] Hildur Einarsdóttir, Magnus Karlsson, Johan Wejde, and Henrik CF Bauer. Diffusion-weighted mri of soft tissue tumours. *European radiology*, 14(6):959–963, 2004.

[57] Ramon Ribes Antonio Luna, Jorge A. Soto. *Diffusion MRI Outside the Brain.* Springer, New York, USA, 2012.

[58] Nathalie Just. Improving tumour heterogeneity mri assessment with histograms. *British journal of cancer*, 2014.

[59] Denis Le Bihan. Intravoxel incoherent motion imaging using steady-state free precession. *Magnetic Resonance in Medicine*, 7(3):346–351, 1988.

[60] Catherina SP van Rijswijk, Patrik Kunz, Pancras CW Hogendoorn, Antonïe HM Taminiau, Joost Doornbos, and Johan L Bloem. Diffusion-weighted mri in the characterization of soft-tissue tumors. *Journal of Magnetic Resonance Imaging*, 15(3):302–307, 2002.

[61] Shuji Nagata, Hiroshi Nishimura, Masafumi Uchida, Jun Sakoda, Tatsuyuki Tonan, Kouji Hiraoka, Kensei Nagata, Jun Akiba, Toshi Abe, and Naofumi Hayabuchi. Diffusion-weighted imaging of soft tissue tumors: usefulness of the apparent diffusion coefficient for differential diagnosis. *Radiation medicine*, 26(5):287–295, 2008.

[62] Kiyoshi Oka, Toshitake Yakushiji, Hiro Sato, Shigeta Yorimitsu, Yoshiko Hayashida, Yasuyuki Yamashita, and Hiroshi Mizuta. Ability of diffusion-weighted imaging for the differential diagnosis between chronic expanding hematomas and malignant soft tissue tumors. *Journal of Magnetic Resonance Imaging*, 28(5):1195–1200, 2008.

[63] Daniel M Patterson, Anwar R Padhani, and David J Collins. Technology insight: water diffusion mri?a potential new biomarker of response to cancer therapy. *Nature Clinical Practice Oncology*, 5(4):220–233, 2008.

[64] Kevin C Chen and Charles Nicholson. Changes in brain cell shape create residual extracellular space volume and explain tortuosity behavior during osmotic challenge. *Proceedings of the National Academy of Sciences*, 97(15):8306–8311, 2000.

[65] Michael MY Khoo, Philippa A Tyler, Asif Saifuddin, and Anwar R Padhani. Diffusion-weighted imaging (dwi) in musculoskeletal mri: a critical review. *Skeletal radiology*, 40(6):665–681, 2011.

[66] Dow-Mu Koh and Harriet C Thoeny. *Diffusion-weighted MR imaging: applications in the body*. Springer Science & Business Media, 2010.

[67] Bachir Taouli, Valérie Vilgrain, Erik Dumont, Jean-Luc Daire, Bo Fan, and Yves Menu. Evaluation of liver diffusion isotropy and characterization of focal hepatic lesions with two single-shot echo-planar mr imaging sequences: Prospective study in 66 patients 1. *Radiology*, 226(1):71–78, 2003.

[68] Takeshi Sugahara, Yukunori Korogi, Masato Kochi, Ichiro Ikushima, Yoshinori Shigematu, Toshinori Hirai, Tomoko Okuda, Luxia Liang, Yulin Ge, Yasuyuki Komohara, et al. Usefulness of diffusion-weighted mri with echo-planar technique in the evaluation of cellularity in gliomas. *Journal of Magnetic Resonance Imaging*, 9(1):53–60, 1999.

[69] Michael P Marks, A De Crespigny, Daniel Lentz, Dieter R Enzmann, Gregory W Albers, and Michael E Moseley. Acute and chronic stroke: navigated spin-echo diffusion-weighted mr imaging. *Radiology*, 199(2):403–408, 1996.

[70] Roland Bammer. Basic principles of diffusion-weighted imaging. *European journal of radiology*, 45(3):169–184, 2003.

[71] Sergey Ya Proskuryakov, Anatoli G Konoplyannikov, and Vladimir L Gabai. Necrosis: a specific form of programmed cell death? *Experimental cell research*, 283(1):1–16, 2003.

[72] Osamu Yanagisawa, Daisuke Shimao, Katsuya Maruyama, Matthew Nielsen, Takeo Irie, and Mamoru Niitsu. Diffusion-weighted magnetic resonance imaging of human skeletal muscles: gender-, age-and muscle-related differences in apparent diffusion coefficient. *Magnetic resonance imaging*, 27(1):69–78, 2009.

[73] Dow-Mu Koh and David J Collins. Diffusion-weighted mri in the body: applications and challenges in oncology. *American Journal of Roentgenology*, 188(6):1622–1635, 2007.